

CHAPTER 6

RESULTS AND DISCUSSION (PART III):

LEAD MAGNESIUM NIOBATE-LEAD TITANATE

This chapter deals with work carried out to fabricate ceramic-nanocomposite in the PMN-PT system using the bimodal particle size packing concept. In applying this concept, five sets of compositions arise, whereby the dispersed phase of nanosized component cannot have a higher concentration than matrix phase counterpart. Between the two end components (i.e. PMN and PT), it was decided to employ PT nanopowders as dispersed phase owing to its easier perovskite formation and higher internal stress. As a first stage, comprehensive study of optimizing the vibro-milling time, thereby demonstrating the validity of the mechanical powder-processing for the production of PT nanopowders was investigated. Finally, phase formation, microstructure, electrical properties and thermal expansion of the ceramic-nanocomposites in the PMN-PT system were investigated.

6.1 Lead Titanate Nanopowders

It is appropriate here to investigate the effect of vibro-milling time (ranging from 0.5-35 h) on phase formation and particle size of PT powders. Each of the powders milled for different times were calcined at various temperatures and dwell times, followed by phase analysis using XRD. The crystalline size, lattice strain and tetragonality (c/a) were estimated from these XRD patterns.

TG and DTA results for the powders milled at different times are compared and shown in Figs. 6.1 and 6.2, respectively. In general, similar thermal

characteristics are observed in all cases. As shown in Fig. 6.1, all powders demonstrate two distinct weight losses below 400 °C. The first weight loss occurs below 100 °C and the second one above 200 °C. In the temperature range from room temperature to ~ 150 °C, all samples show exothermic peaks in the DTA curves at 120 °C (Fig. 6.2), which are related to the first weight loss. These DTA peaks can be attributed to the decomposition of the organic species originating from the milling process [64]. Corresponding to the second fall in specimen weight, by increasing the temperature up to ~ 800 °C, the solid-state reaction between lead oxide and titanium oxide occurs. The broad exothermic characteristic present in all the DTA curves represents that reaction, which has a maximum at ~ 600-750 °C. The slightly different temperature, intensities and shapes of the thermal peaks for the powders are probably related to the different sizes of the powders subjected to different milling times and, consequently, caused by the removal of organic species and rearrangement of differently bonded species in the network [182]. No further significant weight loss was observed for temperatures above 500 °C in the TGA curves, indicating that the minimum firing temperature to form PbO-TiO₂ compounds is in good agreement with XRD results (Fig. 6.3) and those of previous authors [46,174].

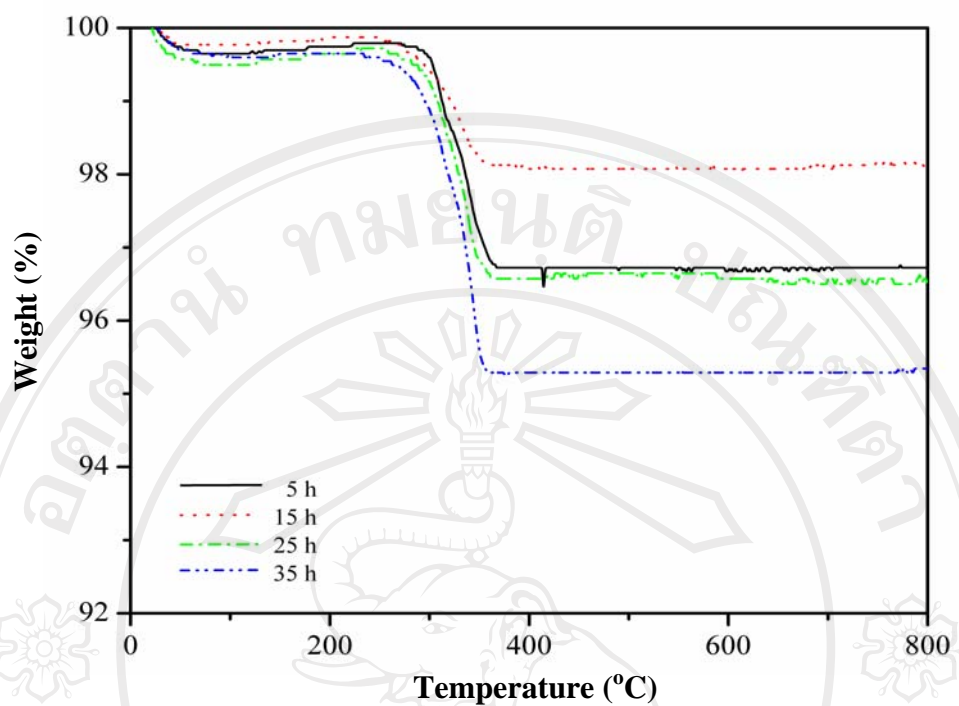


Fig. 6.1 TG analysis of the PbO-TiO₂ mixtures milled at different times.

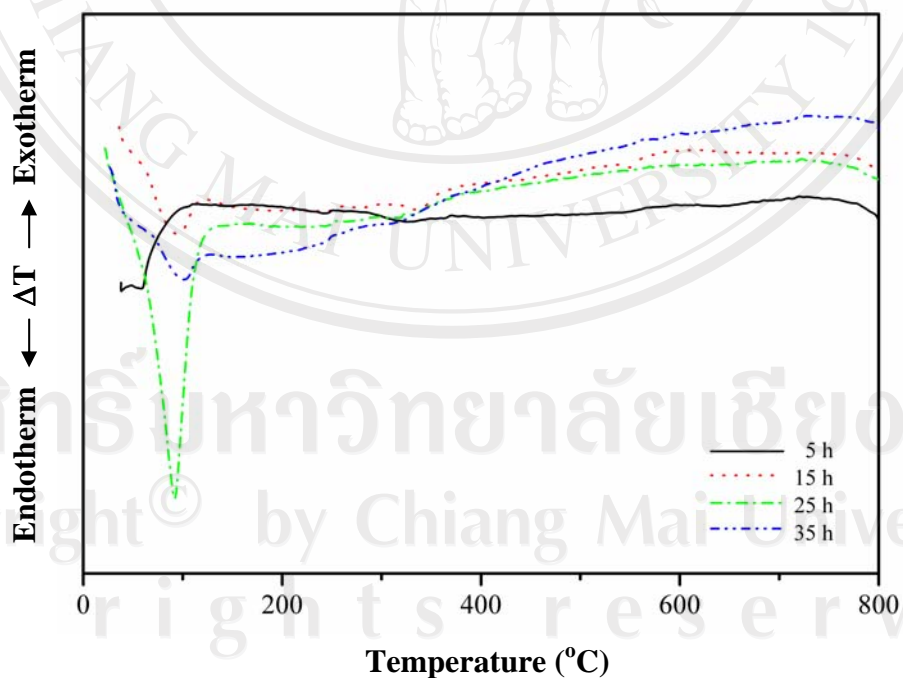


Fig. 6.2 DTA analysis of the PbO-TiO₂ mixtures milled at different times.

To further study the effect of milling time on phase formation, each of the powders milled for different times were calcined at 600 °C for 2 h in air, followed by phase analysis using XRD. For the purpose of estimating the concentrations of the phase present, Eq. (3.9) has been applied to the powder XRD patterns obtained, as given in Table 6.1. As shown in Fig. 6.3, for the uncalcined powder subjected to 0.5 h of vibro-milling, only X-ray peaks of precursors PbO (▼) and TiO₂ (*) are present, indicating that no reaction had been initiated during the milling process. However, after calcinations at 600 °C, it is seen that the perovskite-type PT becomes the predominant phase in the powder milled for 0.5 h indicating that the reaction has occurred to a considerable extent. It is seen that ~ 11 wt% of lead deficient phase, PbTi₃O₇ (▽), reported by a number of workers [174,175] has been found only at a milling time of 0.5 h. This pyrochlore phase has a monoclinic structure with cell parameters $a = 1.07 \text{ \AA}$, $b = 3.81 \text{ \AA}$, $c = 6.58 \text{ \AA}$ and $\beta = 98.08^\circ$ (JCPDS file no. 21-949) [183]. This observation could be attributed mainly to the poor mixing capability under short milling time. With milling time of 1 h or more, it is apparent that a single phase perovskite PT (yield of 100% within the limitations of the XRD technique) was found to be possible after the same calcination process was applied.

In general, the strongest reflections found in the majority of these XRD patterns indicate the formation of PT. These can be matched with JCPDS file no. 6-452 for the tetragonal phase, in space group $P4/mmm$ with cell parameters $a = 3.90 \text{ \AA}$ and $c = 4.15 \text{ \AA}$ [171], in consistent with other works [64,172]. It should be noted that no evidence for the introduction of impurity due to wear debris from the milling process was observed in any of the calcined powders (within the milling periods of

0.5-35 h), demonstrating the effectiveness of the vibro-milling technique for the production of high purity PT nanopowders.

Moreover, it has been observed that with increasing milling time, all diffraction lines broaden, e.g. (002) and (200) peaks, an indication of a continuous decrease in particle size then also increase after 25 h and of the introduction of lattice strain, as shown in Fig. 6.4. These values indicate that the particle size affects the evolution of crystallinity of the phase formed by prolonged milling treatment (Fig. 6.5). For PT powders, the longer the milling time, the finer is the particle size, up to a certain level (Table 6.1). The results suggest that the steady state of the vibro-milling is attained at ~ 20 h of milling. Moreover, it is worthy to note that, in this condition, the mean crystalline size is close to ~ 21 nm. Also, the relative intensities of the Bragg peaks and the calculated tetragonality factor (c/a) for the powders tend to decrease with the increase of milling time. However, it is well documented that, as Scherer's analysis provides only a measurement of the extension of the coherently diffracting domains, the particle sizes estimated by this method can be significantly underestimated [184]. In addition to strain, factors such as dislocations, stacking faults, heterogeneities in composition and instrumental broadening can contribute to peak broadening, making it almost impossible to extract a reliable particle size solely from XRD [137,185].

Table 6.1 Effect of milling time on the variation of particle size of PT powders measured by different techniques after calcined at 600 °C for 2 h with heating/cooling rates of 20 °C/min.

Milling Time (h)	PT phase (%)	XRD		SEM		Laser scattering	
		A (nm)	<i>c/a</i>	D (nm)	P (nm)	D (nm)	P (nm)
0.5	89.20	40	1.056	145	40-250	1090	140-2560
1	100	20.8	1.062	107	71-143	660	270-1090
5	100	22.5	1.059	101	67-135	690	290-1140
10	100	21.9	1.059	95	63-128	690	290-1140
15	100	22.0	1.061	78	43-114	4640	1640-7790
20	100	21.3	1.056	68	28-109	4800	1710-8060
25	100	21.5	1.057	63	17-109	180	70-310
30	100	21.5	1.052	93	43-143	170	70-290
35	100	21.4	1.053	92	56-128	3030	560-6180

A = Crystalline size

c/a = Tetragonality factor

D = Average particle size

P = Particle size distribution or range

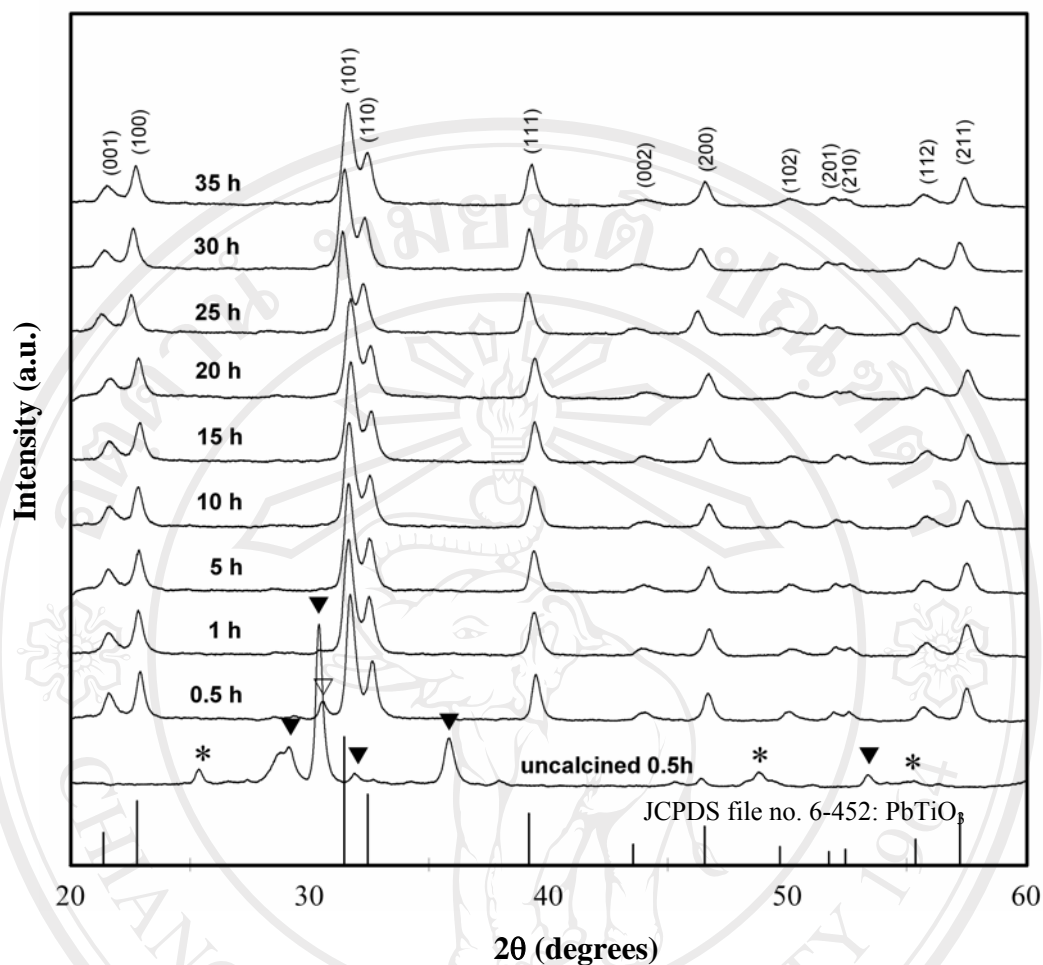


Fig. 6.3 XRD patterns of PT powders milled at different times (calcined at 600 °C for 1 h with heating/cooling rates of 20 °C/min) (▼ PbO, * TiO₂ and ∇ PbTi₃O₇).

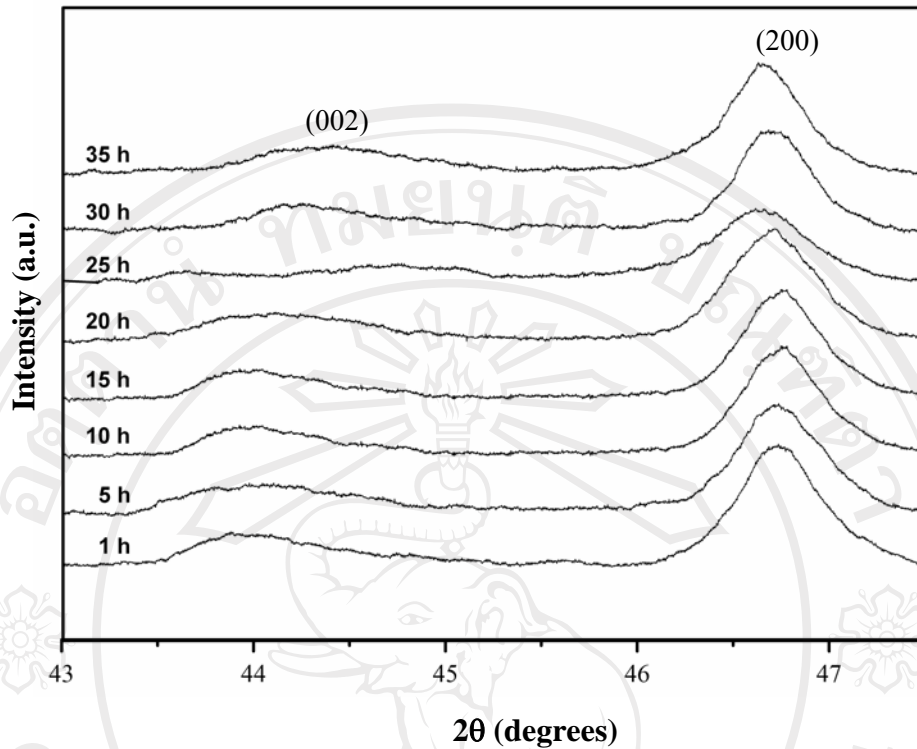


Fig. 6.4 Enlarged zone of XRD patterns showing (002) and (200) peaks broadening as a function of milling times.

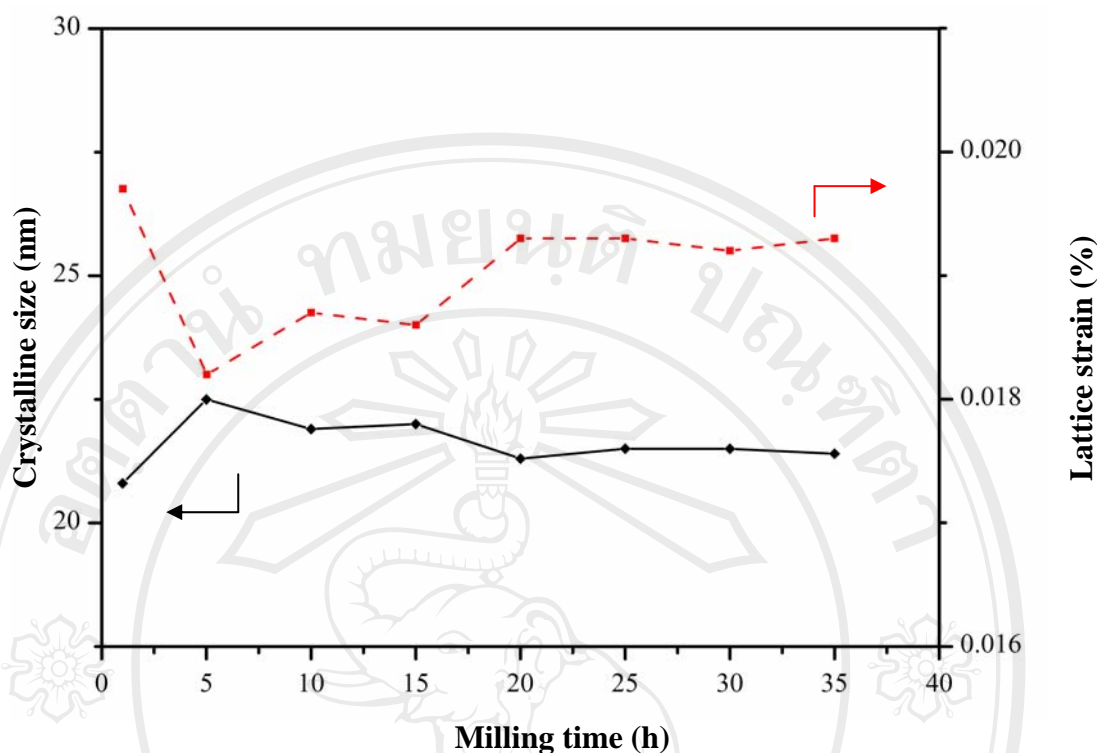


Fig. 6.5 Variation of crystalline size and lattice strain of PT powders as a function of milling times.

For 20 h of milling, after calcination at 500 and 550 °C, it is seen that the perovskite-type PT becomes the predominant phase indicating that the reaction has occurred to a considerable extent. Further calcination at 550 °C with dwell time of 1 h or more does not result in a very much increase in the amount of PT whereas the traces of unreacted PbO and TiO₂ could not be completely eliminated (Fig. 6.6). This could be attributed to the poor reactivity of lead and titanium species [172]. However, it should be noted that after calcination at 600 °C for 2 h, the single phase of perovskite PT (yield of 100% within the limitations of the XRD technique) was obtained.

To further study the phase development with increasing milling times, an attempt was also made to calcine mixed powders milled at 25 h and 30 h under various conditions as shown in Figs. 6.7 and 6.8, respectively. In this connection, it is seen that by varying the calcination temperature, the minimum firing temperature for the single phase formation of each milling batch is gradually decreased with increasing milling time (Figs. 6.6-6.8). The main reason for this behavior is that a complete solid-state reaction probably takes place more easily when the particle size is milled down to accelerate an atomic diffusion mechanism resulting in the suitable level of homogeneous mixing. It is therefore believed that the solid-state reaction to form perovskite PT phase occurs at lower temperatures with decreasing the particle size of the oxide powders.

From Figs. 6.7 and 6.8, it is clear that the intensity of the perovskite peaks was further enhanced when the dwell times of the calcination process were extended up to 3 h at the expenses of PbO, TiO₂ and PbTi₃O₇ phases. An essentially monophasic PT of perovskite structure was obtained at 550 °C when the calcination time was increased to 3 h and 2 h for the milling time of 25 h and 30 h, respectively, as shown in Figs. 6.7 and 6.8 (c). This was apparently a consequence of the enhancement in crystallinity of the perovskite phase with increasing degree of mixing and dwell time, in good agreement with other works [174,175].

An attempt was also made to calcine the powders with 30 h of milling times under various heating/cooling rates (Fig. 6.8). In this connection, it is shown that the yield of PT phase did not vary significantly with different heating/cooling rates ranging from 5 to 30 °C/min, in good agreement with the early observation for the PT powders subjected to 0.5 h of vibro-milling times [172]. It should be noted that no

evidence of the introduction of impurity due to wear debris from the selected milling process was observed in all calcined powders, indicating the effectiveness of the vibro-milling technique for the production of high purity PT nanopowders.

The variation of calculated crystallite size, tetragonality factor (c/a) and lattice strain of the powders milled for different times with the calcination conditions is given in Table 6.2. In general, it is seen that the crystallite size of PT decreases slightly with increasing calcination temperature for all different milling times, while the calculated values of the tetragonality factor and mean lattice strain progressively increase. However, it should be noted that by increasing the calcination time from 1 to 3 h, these calculated values decrease to the minimum at 2 h and then grow up further after longer dwell time was applied. There is no obvious interpretation of these observations, although it is likely to correspond to the competition between the major mechanisms leading to crystallization and agglomeration [175].

Table 6.2 Effect of calcination conditions on the variation of crystalline size, tetragonality factor (c/a) and mean lattice strain of PT powders milled for different times.

Calcination condition $T/D/R$ ($^{\circ}\text{C}/\text{h}/^{\circ}\text{Cmin}^{-1}$)	Crystalline size (nm)	Lattice strain (%)	Tetragonality factor (c/a)
500/2/30	21.8	0.0188	1.038
550/1/30	19.4	0.0212	1.055
550/2/30	21.6	0.0190	1.052
550/3/30	20.9	0.0197	1.054
600/2/30	21.5	0.0193	1.057

T = Calcination temperature

D = Dwell time

R = Heating/cooling rates

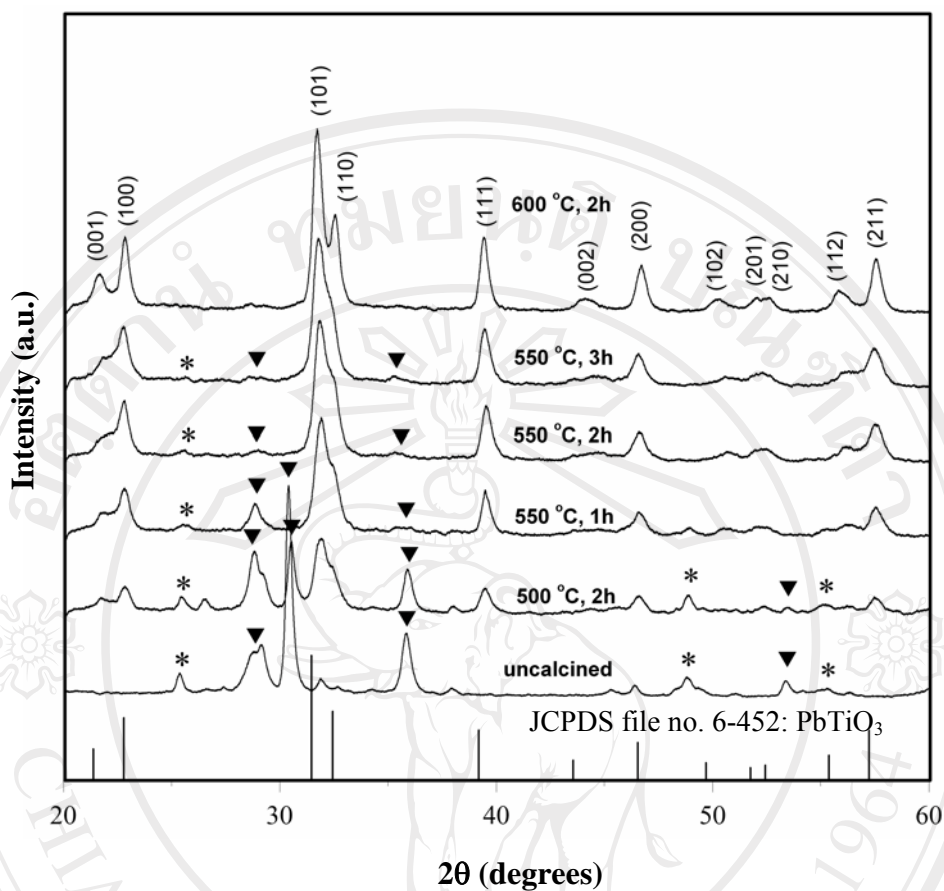


Fig. 6.6 XRD patterns of PT powders milled for 20 h and calcined at various conditions.

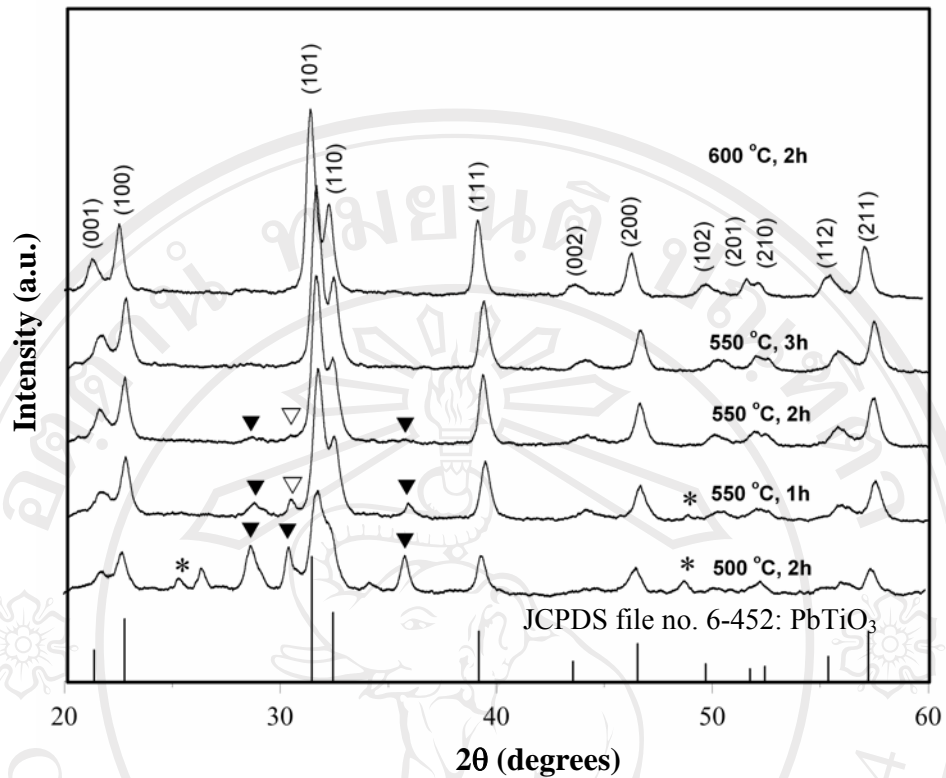


Fig. 6.7 XRD patterns of PT powders milled for 20 h and calcined at various conditions.

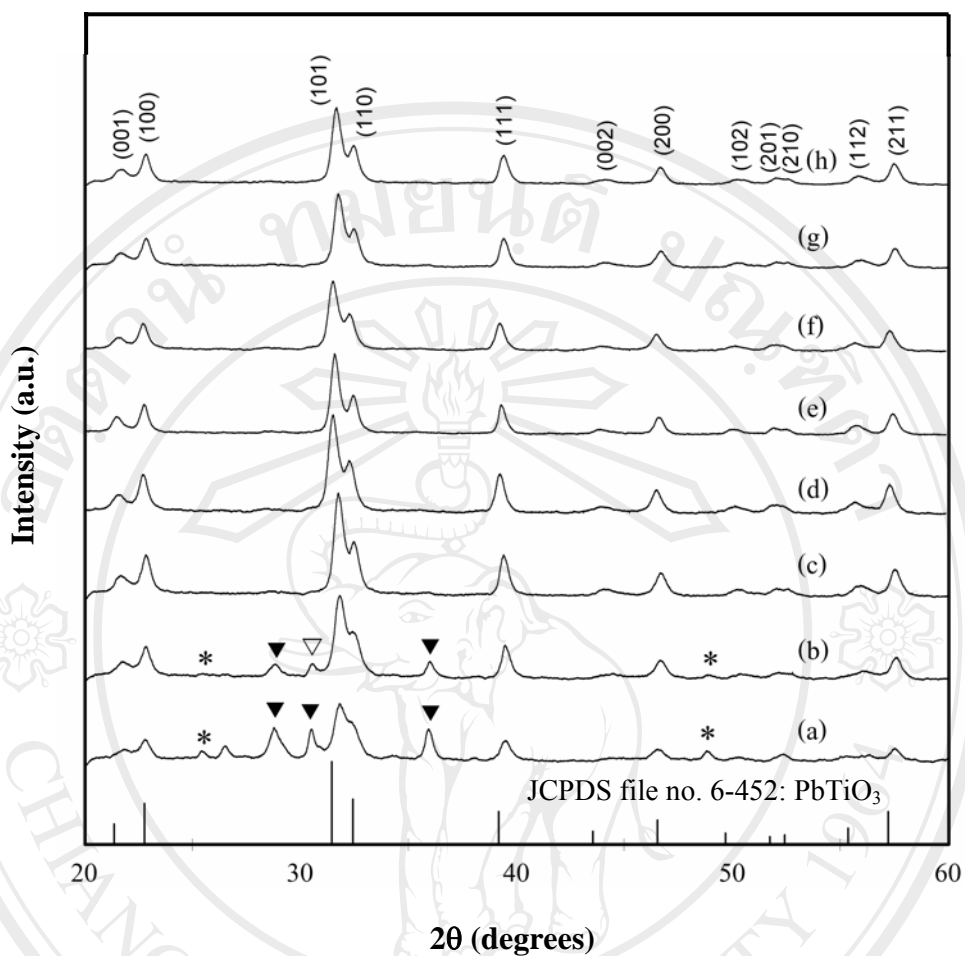
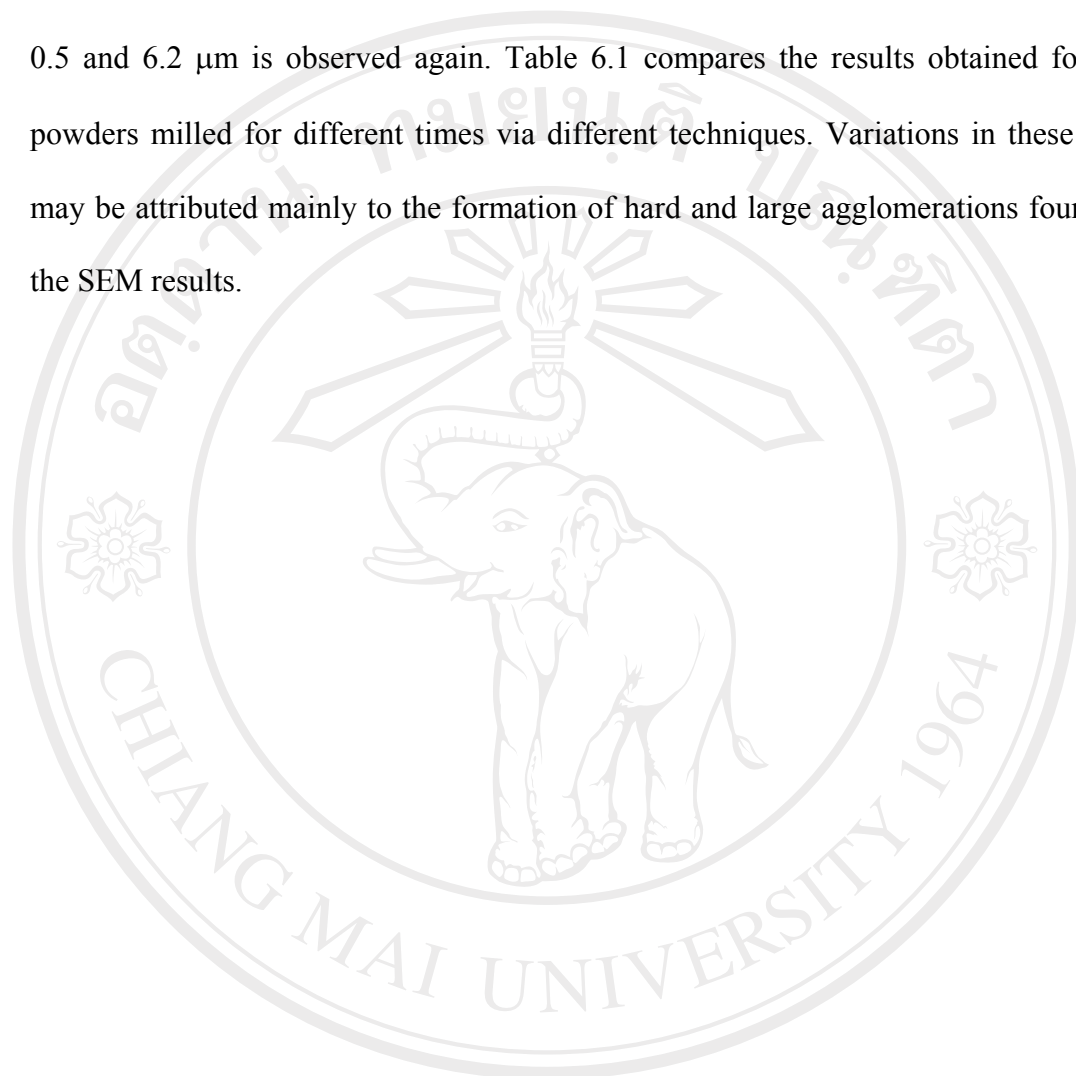


Fig. 6.8 XRD patterns of PT powders milled for 30 h and calcined at (a) 500 °C for 2 h, (b) 550 °C for 1 h, (c) 550 °C for 2 h, (d) 550 °C for 3 h, (e) 600 °C for 2 h, with heating/cooling rates of 5 °C/min and 550 °C for 3 h with heating/cooling rates of (f) 10 °C/min, (g) 20 °C/min and (h) 30 °C/min.

In this connection, scanning electron microscopy was also employed for particle size measurement (Table 6.1). The morphological evolution of the powders as a function of milling time was also revealed, as illustrated in the SEM micrographs (Fig. 6.9). At first sight, the morphological characteristic of PT powders with various milling times is similar for all cases. In general, the particles are agglomerated and basically irregular in shape, with a substantial variation in particle sizes. The powders consist of primary particles nanometers in size. Increasing the milling time over the range 0.5 to 35 h, the average size of the PT particle decreases significantly, until at 25 h, the smallest particle size (estimated from SEM micrographs to be ~ 17 nm) is obtained. However, it is also of interest to point out that a larger particle size was obtained for a milling time longer than 25 h. This may be attributed to the occurrence of hard agglomeration with strong inter-particle bonds within each aggregate resulting from dissipated heat energy of prolonged milling [186]. Fig. 6.9 also illustrates that vibro-milling has slightly changed the shape of the particles which become more equiaxed at long milling times. At the same time, the particle size is reduced. Fracture is considered to be the major mechanism at long milling times.

The effect of milling time on particle size distribution was found to be significant, as shown in Fig. 6.10. After milling times of 1, 5 and 10 h, the powders have a similar particle size distribution. They exhibit a single peak covering the size ranging from 0.2 to 1.1 μm . With increasing milling times to 15 and 20 h, the distribution curve of particle size separates into two groups. First is a monomodal distribution corresponding to the primary size of the PT particles. The second group (peak) is believed to arise mainly from particle agglomeration. By increasing the milling time to 25 and 30 h, a uniform particle size distribution with a much lower

degree of particle agglomeration ($< 1 \mu\text{m}$) is found. However, upon further increase of milling time up to 35 h, a bimodal distribution curve with peak broadening between 0.5 and 6.2 μm is observed again. Table 6.1 compares the results obtained for PT powders milled for different times via different techniques. Variations in these data may be attributed mainly to the formation of hard and large agglomerations found in the SEM results.



ลิขสิทธิ์มหาวิทยาลัยเชียงใหม่

Copyright© by Chiang Mai University

All rights reserved

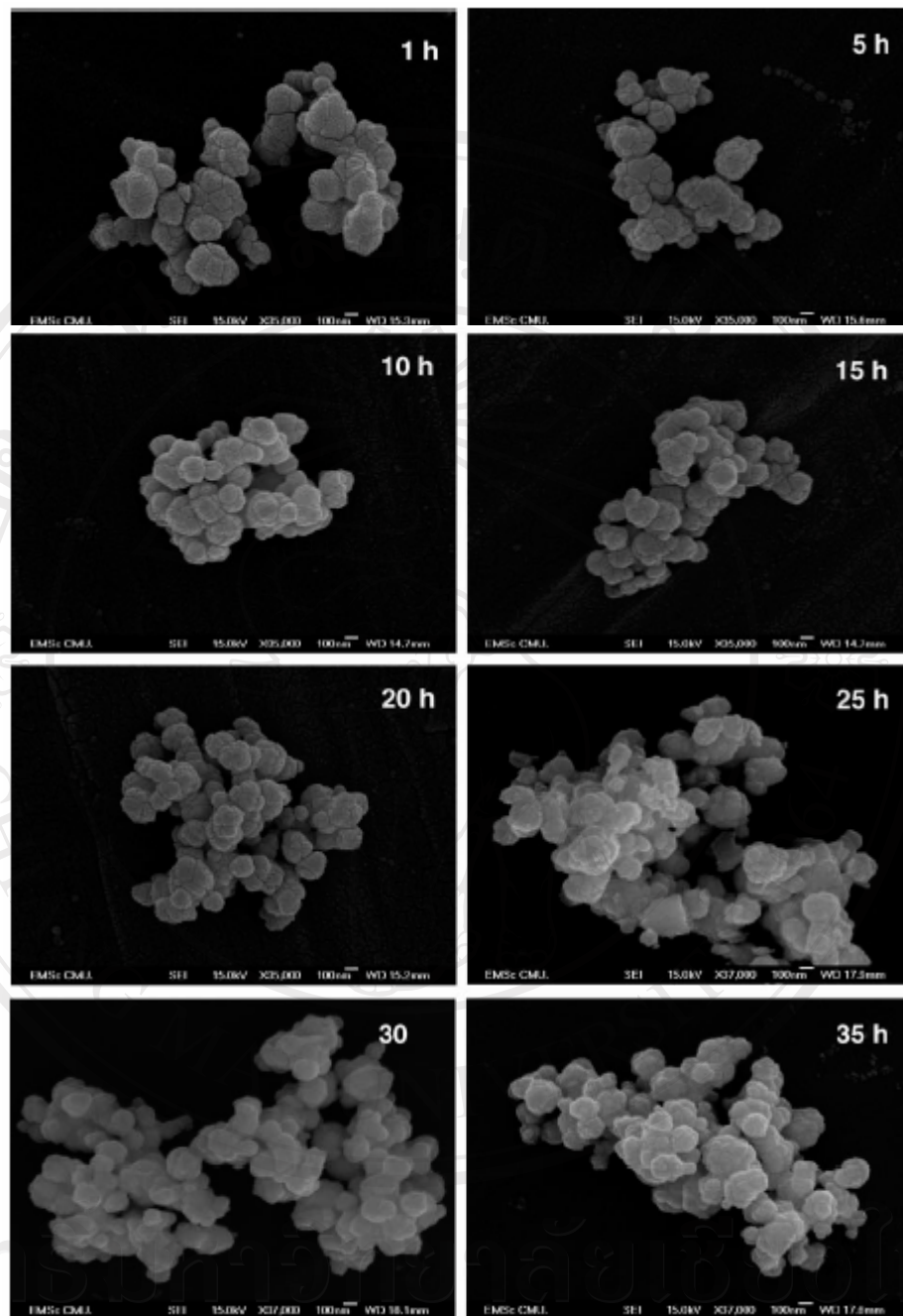


Fig. 6.9 SEM micrographs of PT powders milled at different times.

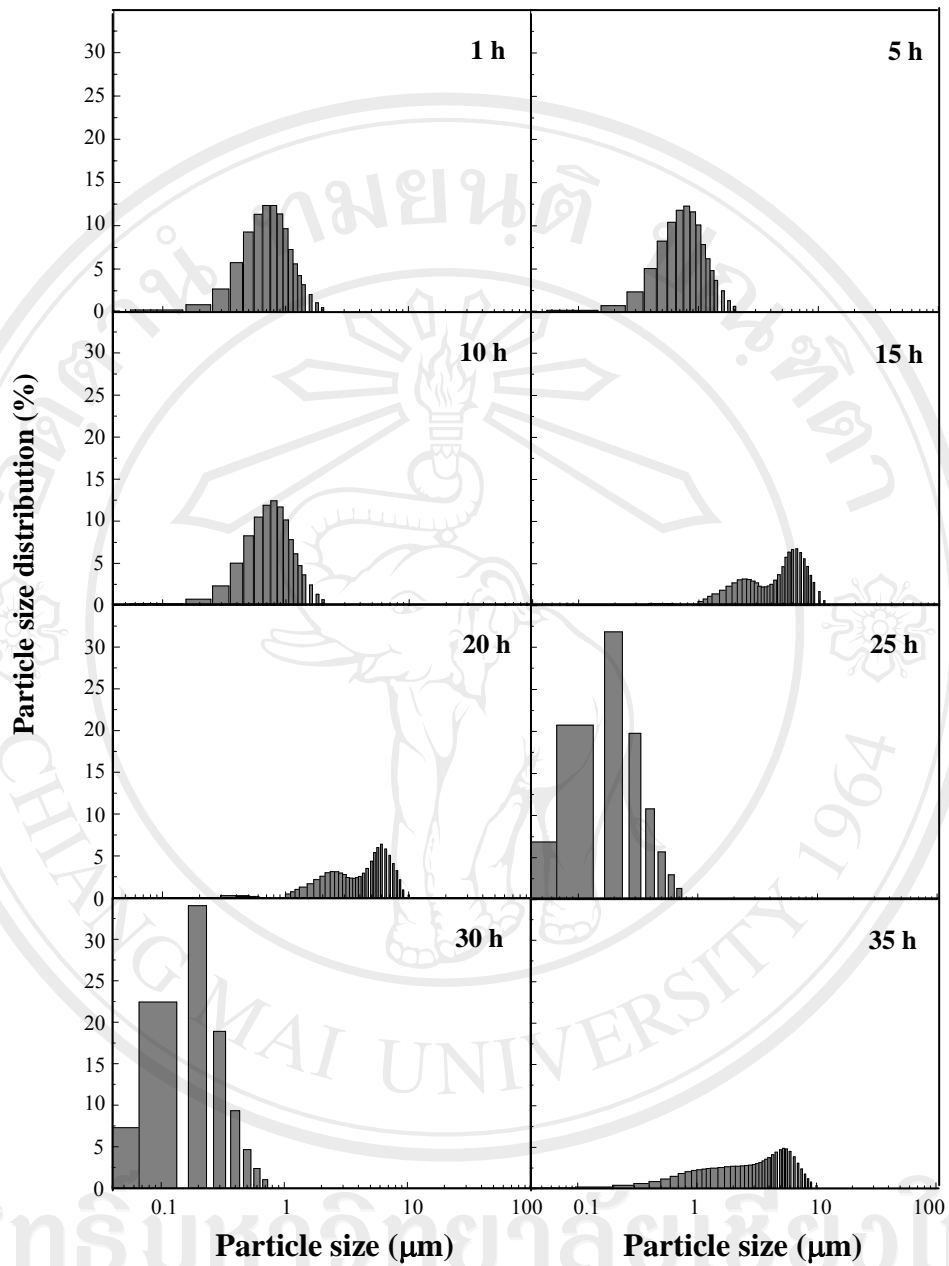


Fig. 6.10 Particle size distributions of PT powders milled at different times.

ลิขสิทธิ์มหาวิทยาลัยเชียงใหม่
Copyright © by Chiang Mai University
All rights reserved

A TEM bright field image of an agglomerated or intergrown particle of the calcined PT powders derived from milling time of 25 h is shown in Fig. 6.11 (a). By employing the selected area electron diffraction (SAED) technique, a perovskite-like phase of tetragonal $P4/mmm$ PT is identified (Fig. 6.11 (b)), in good agreement with the XRD analysis and the data in JCPDS file no. 6-452 [171]. The reciprocal lattice pattern of this PT phase was also simulated with the Carine Crystallography 3.0 software, as demonstrated in Fig. 6.11 (c).

The results infer that the milling time influences not only on the development of the solid-state reaction of PT phase but also the particle size and morphology. The resulting PT powders have a range of particle size, depending on milling times. Production of a single-phase PT nanopowder can be successfully achieved by employing a combination of 25 h milling time and calcination conditions of 600 °C for 2 h, with heating/cooling rates of 20 °C min⁻¹. Therefore, in the next sections, PT nanopowders were used for the fabrication of PMN-PT ceramic-nanocomposites.

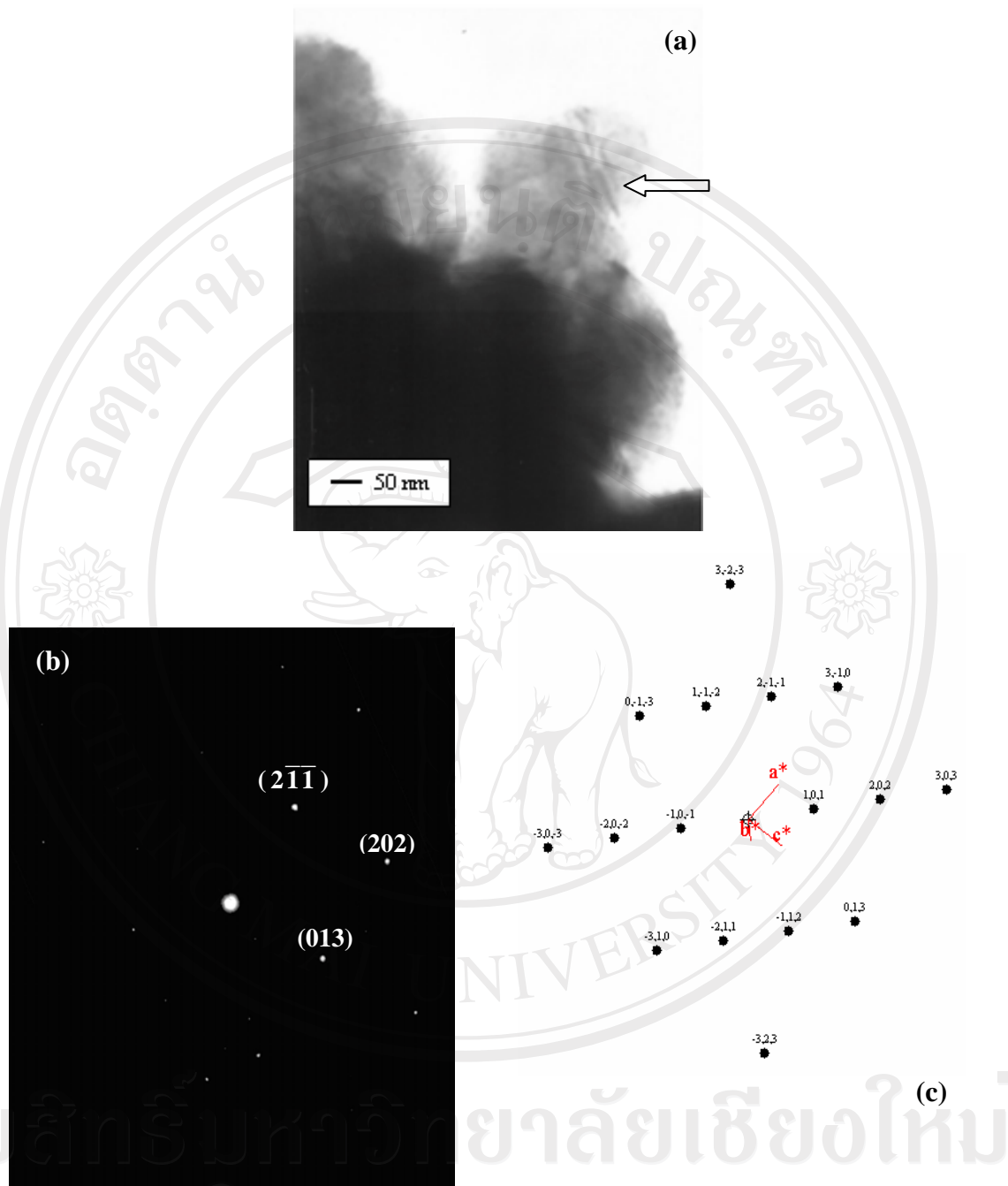


Fig. 6.11 (a) TEM micrograph, (b) SAED pattern ($[1\bar{3}1]$ zone axis) and (c) reciprocal lattice pattern simulation of PT powders milled for 25 h and calcined at 600 °C for 2 h with heating/cooling rates of 30 °C/min.

6.2 PMN-PT Ceramic-Nanocomposites

Ceramic-nanocomposites in the system $(1-x)\text{PMN}-x\text{PT}$ ($0.1 \leq x \leq 0.5$; $\Delta x = 0.1$) have been fabricated from PMN powders (section 4.1.2) and PT nanopowders (section 6.1), employing a normal sintering method previously advocated by Udornporn [187]. Attention was focused on relationships between chemical composition, densification, microstructure, electrical properties and thermal expansion. The X-ray diffraction patterns from sintered PMN-PT ceramic-nanocomposites sintered at $1100\text{ }^\circ\text{C}$ are given in Fig. 6.12, where the perovskite structure was formed throughout the whole composition ranges. In general, only a pseudo-cubic symmetry was observed at low values of PT concentration, in good agreement with other workers [188,189]. By the influence of PT, however, several peaks split for $x \geq 0.3$, indicating the development of tetragonal symmetry, which continued with a further increase in PT concentration. For example, (002)/(200) peaks splitting the diffraction line around 2θ of $44\text{-}46^\circ$ are shown in Fig. 6.13 confirming their tetragonal symmetry.

The densification data of all compositions, compared with PMN-PT ceramic-nanocomposites sintered at $1250\text{ }^\circ\text{C}$ is given in Table 6.3. In general, the bulk density was found to increase slightly with x content, which could be due to the lower melting point of PT compared to PMN [88,95]. Thus, the admixture of PMN could be considered as a useful technique for promoting the densification of PT, along with its other significant advantage of bringing the Curie range down to lower temperatures as demonstrated by a number of workers [35,88,190]. Densities of about $4.74\text{-}7.28\text{ g/cm}^3$ (Fig. 6.14) were obtained, which are considerably lower than the values obtained for sintered PMN-PT solid-solution ceramics [187]. Moreover, these density values are

also lower than the values in ceramics sintered at 1250 °C. In order to preserve the ceramics with nanostructural arrangement, it is possible that the employed sintering temperature in this work is not enough for driving densification mechanism to achieve dense PMN-PT ceramic-nanocomposites. However, the scope for improving pressureless sintering by raising the temperature is limited by the melting point of both Pb-containing perovskite components PMN and PT. Furthermore, in Table 6.3, it can be seen that grain sizes of ceramic-nanocomposites sintered at low temperature are smaller than those obtained in ceramics sintered at higher temperature. Besides the effect of sintering temperature can cause to occur these results, other reason which is possible, is that the incorporation of second phase could limit grain growth in the matrix.

Table 6.3 Phase and densification characteristics of $(1-x)$ PMN- x PT ceramic-nanocomposites from sintered at different temperatures..

Composition (x)	Sintering temperature (°C)					
	1100			1250		
	Perovskite phase (%)	Density (g/cm ³)	Grain size (μ m)	Perovskite phase (%)	Density (g/cm ³)	Grain size (μ m)
0.1	100	4.74	0.09-1.95	100	7.06	0.53-3.67
0.2	100	5.92	0.18-1.94	100	7.10	0.33-3.34
0.3	100	6.59	0.08-1.54	100	7.20	0.52-3.53
0.4	100	7.03	0.10-2.73	100	7.23	0.41-4.02
0.5	100	7.28	0.09-3.00	100	7.40	0.67-3.13

^aThe estimated precision of the density is ± 0.05 g/cm³

^bThe estimated precision of the grain size is ± 0.05 μ m

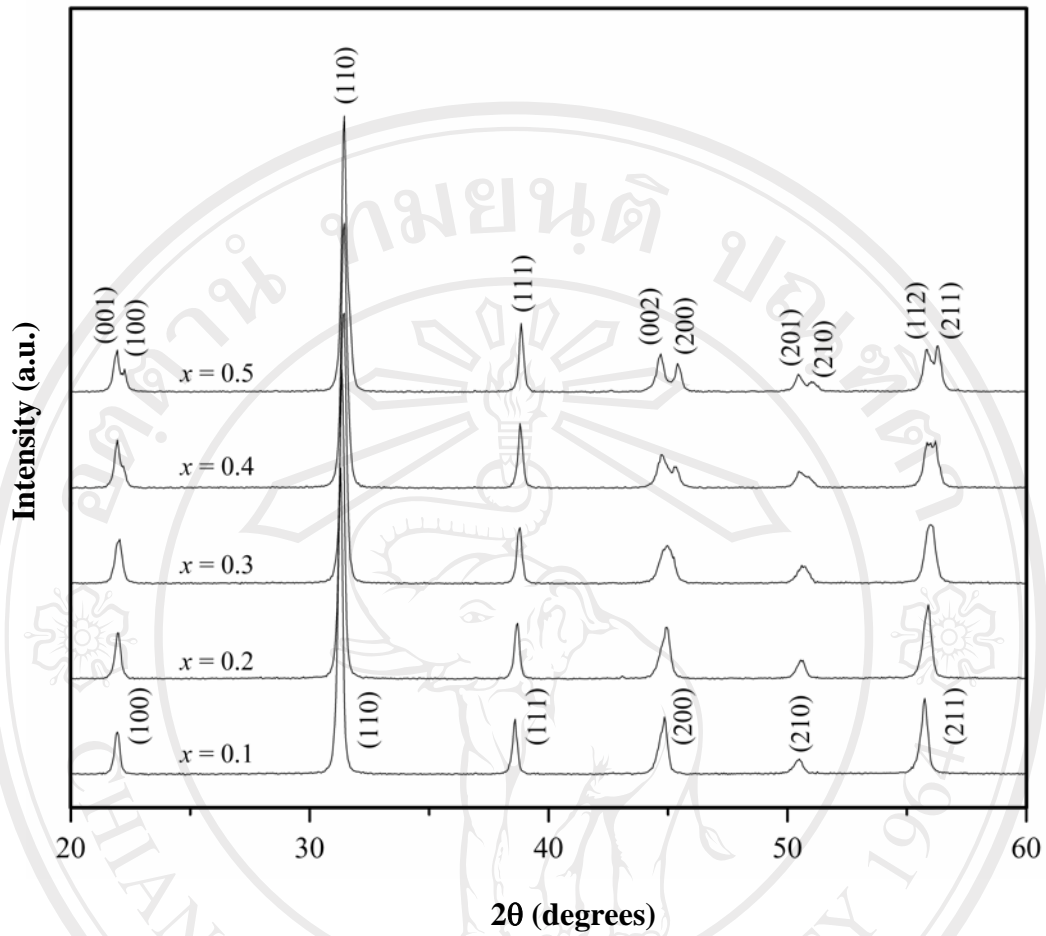


Fig. 6.12 XRD patterns of the $(1-x)\text{PMN}-x\text{PT}$ ceramic-nanocomposites sintered at 1100°C for 2 h with heating/cooling rates of $5^\circ\text{C}/\text{min}$.

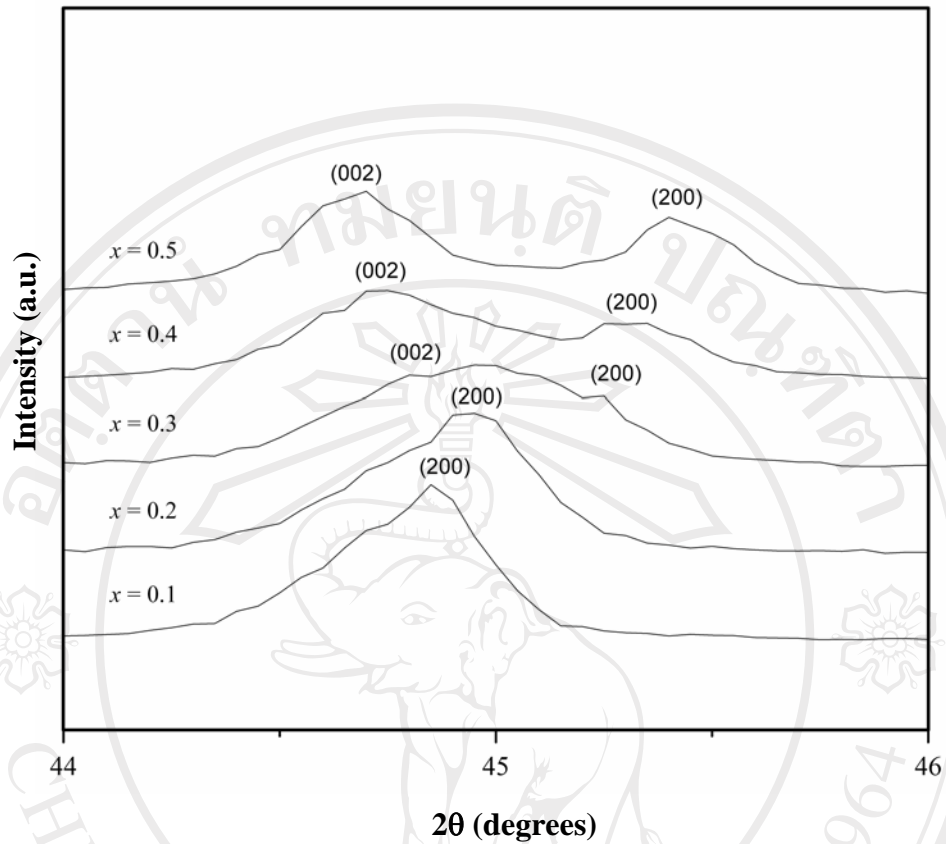


Fig. 6.13 XRD patterns of (002)-(200) reflections for the $(1-x)$ PMN- x PT ceramic-nanocomposites with different x -values.

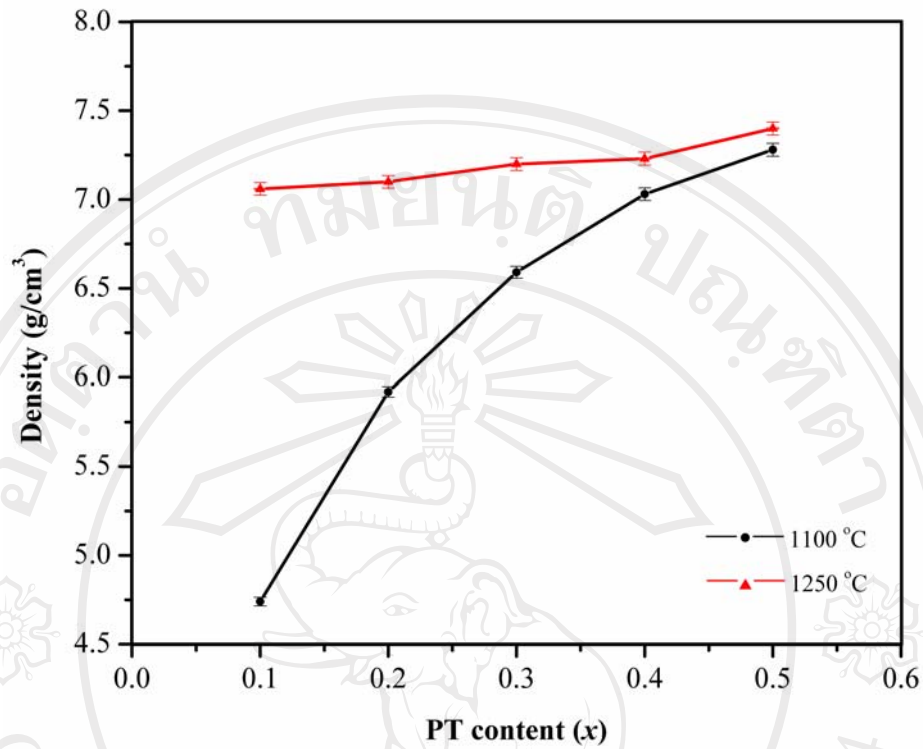


Fig. 6.14 Variation of density with compositions for (1-x)PMN-xPT ceramic-nanocomposites.

SEM micrographs of $(1-x)\text{PMN}-x\text{PT}$ ceramic-nanocomposites ($x = 0.1, 0.3$ and 0.5) sintered at different temperatures are compared as given in Fig. 6.15 (a-f). In general, the sample shows nearly 100% intergranular fracture behavior. With increasing PT content, the grain boundary changed from intergranular to transgranular surface (Fig. 6.5 (c)). It can be also seen that the sample only has a few of small pores at grain boundaries and triple points; cracks or microcracks were not detected. Moreover, a degree of grain close-packing microstructures tends to increase with x content. High porosity and heterogeneous microstructures consisting mainly of two ranges of particles (in respect of size and shape) were found in the samples sintered at lower temperature (Fig. 6.15 (a)-(c)). A distribution of very small particles with diameter $\sim 100\text{-}200$ nm is found over the PMN grains. Large pore-sizes of the order of $1\ \mu\text{m}$ were also observed. These poorly sintered samples could be attributed to several factors, including the effect of different size fractions between the two different end components, ineffective mixing, and the use of shortened sintering time or low firing temperature, similar with those observed by Zhang [192]. By comparison with the samples sintered at higher temperatures (Fig. 6.15 (d)-(f)), different microstructural characteristics are clearly observed.

It should be noted that the microstructure of PMN-PT ceramics-nanocomposites sintered at $1100\ \text{°C}$ are totally different from those observed in the solid-solution case [187]. On the other hand, the samples sintered at $1250\ \text{°C}$ show similar microstructure with the solid-solution samples. All samples exhibit uniformly sized grains with a high degree of grain close-packing. Here, the employed sintering temperature is probably high enough for driving diffusion mechanism to achieve the final sintered samples as obtained by the solid-state sintering in the PMN-PT solid-

solution. Clearly, the ceramic fabrication technique has been found to have a pronounced effect on the phase formation, densification and microstructure of ceramics in the PMN-PT system. As shown in Fig. 6.15, two different phases appear in the microstructure, i.e. PMN grains and intergranularly located PT nanoparticles. This kind of microstructure can be matched with the “inter-intragranular” structural model of ceramic-nanocomposites proposed by Niihara *et al.* [122]. Thus, one of the main objectives regarding the fabrication of PMN-PT ceramic-nanocomposites by using the bimodal particle size packing concept (micron sized PMN + nanosized PT powders) is successfully achieved. This type of ceramic-nanocomposite is expected to exhibit good resistance to high temperature creep via the intergranular structure due to grain boundary pinning. Correspondingly, the intragranular configuration hinders crack motion through the grain, i.e. transgranular fracture and potentially the strength and toughness can be enhanced [122]. However, the rationalization of the various mixed-phase sintering phenomena relies on both physical and chemical factors. The physical factors involve the green powder structure, particle size, particle shape, composition, homogeneity and green density [193]. For example, a mixture will exhibit a high packing density when there is a large size difference between the particles. In turn, sintering shrinkage depends not only on temperature and time, but on composition, particle size, phase connectivity and green density. Hence, mixed particles exhibit widely varying responses to sintering cycles dependent on geometric attributes. It can be seen that so many unanswered questions still remain especially in connection with their electrical and thermal properties. These aspects will be verified in the next section.

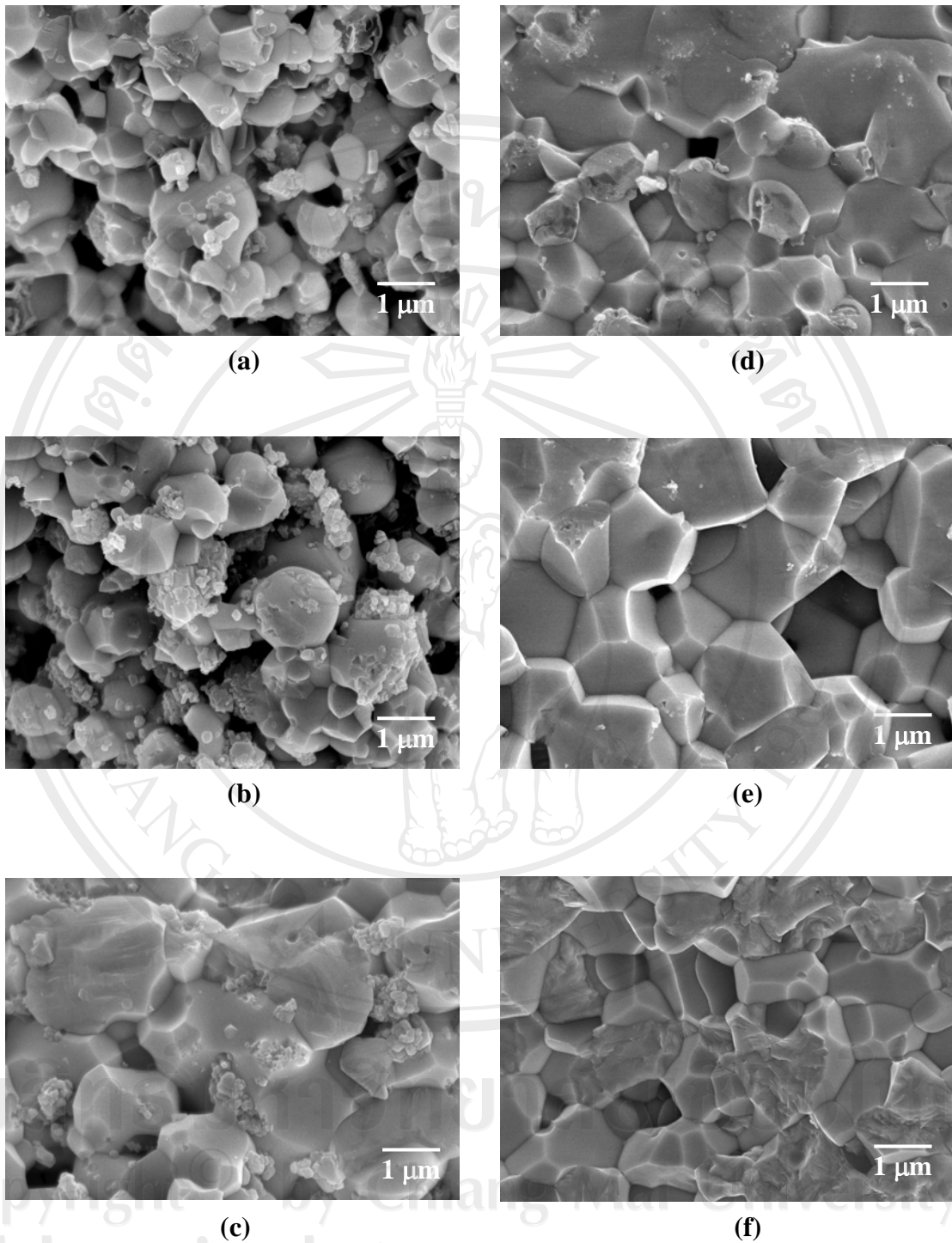


Fig. 6.15 SEM micrographs of the $(1-x)\text{PMN}-x\text{PT}$ ceramic-nanocomposites (a) $x = 0.1$, (b) $x = 0.3$ and (c) $x = 0.5$ after sintered at 1100 °C for 2 h, and (d) $x = 0.1$, (e) $x = 0.3$ and (f) $x = 0.5$ after sintered at 1250 °C for 2 h.

The dielectric properties, e.g. dielectric constant (ϵ_r) and dielectric loss tangent ($\tan\delta$), are measured as functions of both temperature and frequency, as shown in Figs. 6.16 and 6.17. As listed in Table 6.4, the Curie temperature (T_C) (determined at measuring frequency of 1 kHz) increases from 33 °C in 0.9PMN-0.1PT to 270 °C in 0.5PMN-0.5PT. This is a direct result of PT addition to PMN ($T_C \sim -8$ °C) since PT itself has a Curie temperature of 490 °C [15]. As shown in Fig. 6.16 (a) and (b), for 0.9PMN-0.1PT ceramic-nanocomposite, both ϵ_r and $\tan\delta$ exhibits strong temperature-frequency dependence below the transition temperature. This is a typical behavior of relaxor ferroelectrics [169], in which strong temperature-frequency dependence is observed and the temperatures of maximum dielectric constant and dielectric loss tangent are shifted to higher temperature with increasing frequency. The maximum value of the dielectric constant decreases with increasing frequency, while that of the dielectric loss tangent increases. The dielectric properties then become frequency independence above the transition temperature. PMN is a well-known relaxor ferroelectric material as a result of a short-range ordered structure with a nanometer scale heterogeneity in composition [83]. Small addition of PT to PMN causes an increase in T_C , but the strong relaxor behavior still exists. In addition, since 0.9PMN-0.1PT ceramic has a pseudo-cubic symmetry it is therefore intrinsically electrostrictive (i.e. its electrically-induced strain is quadratically proportional to the applied electric field and is non-hysteretic, as shown later in Fig. 6.18) [194]. With its enhanced dielectric properties at room temperature, as listed in Table 6.4, it is widely employed in transducers and actuators [169].

Further increase in PT contents leads to more observable normal ferroelectric behavior because PT is intrinsically a normal ferroelectric [194]. For instance, the

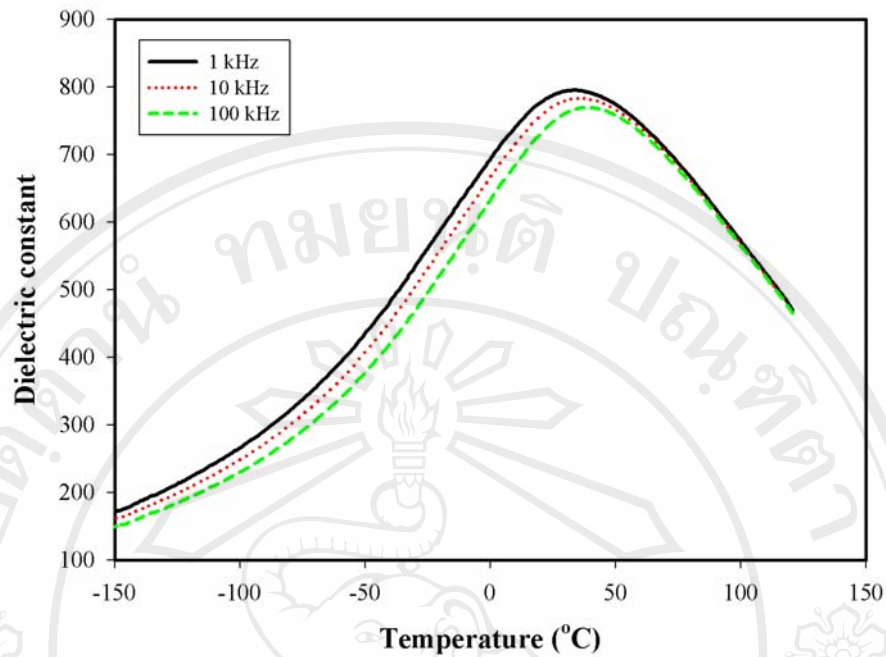
dielectric properties of 0.7PMN-0.3PT ceramic, as plotted in Fig. 6.16 (c) and (d), exhibit a mixture of both normal and relaxor characteristics, in which the transition temperature is not shifted as much as for relaxor 0.9PMN-0.1PT ceramic. Similar tendency has also been observed in several prior investigations [83,195]. It should be noted that 0.7PMN-0.3PT ceramic composition is close to MPB of the PMN-PT system. Therefore, its structural symmetry is a mixture of pseudo-cubic and tetragonal, which in turn causes a mixture of normal and relaxor characteristics observed for dielectric properties. With a tetragonal symmetry, the 0.5PMN-0.5PT ceramic, on the other hand, exhibits a normal ferroelectric behavior (Fig. 6.16 (e) and (f)), in which the dielectric properties change significantly with temperature, but are nearly independent of frequency, except in the vicinity of the phase transformation temperature. This is a typical characteristic of normal ferroelectric ceramics with a long-range ordered structure [83]. It should also be noted here that the dielectric properties in all ceramics increase significantly at high temperature as a result of thermally activated space charge conduction [195]. It can be concluded that when PT is added to form the binary system with PMN, the T_C increases monotonically, as shown in Table 6.4 and Fig. 6.16, and the dielectric behavior is shifted from relaxor ferroelectric towards normal ferroelectric. However, the dielectric constant of ceramic-nanocomposites samples is lower than those values of PMN-PT ceramic-nanocomposites sintered at 1250 °C (as shown in Table 6.4) and solid-solution ceramics for all compositions. There are various reasons for explaining the dielectric response of composite materials. Ausloos *et al.* [196] studied effective dielectric constant theories of composite solids. Their work reported that the broad curve of dielectric constant of the results of clustering effect including the shape of the cluster

and particle heterogeneity effect. In this work, it is possible that PT nanoparticles in the samples may hinder domain wall motion and lead to reduce dielectric constant. Another reason should possible is the low density values.

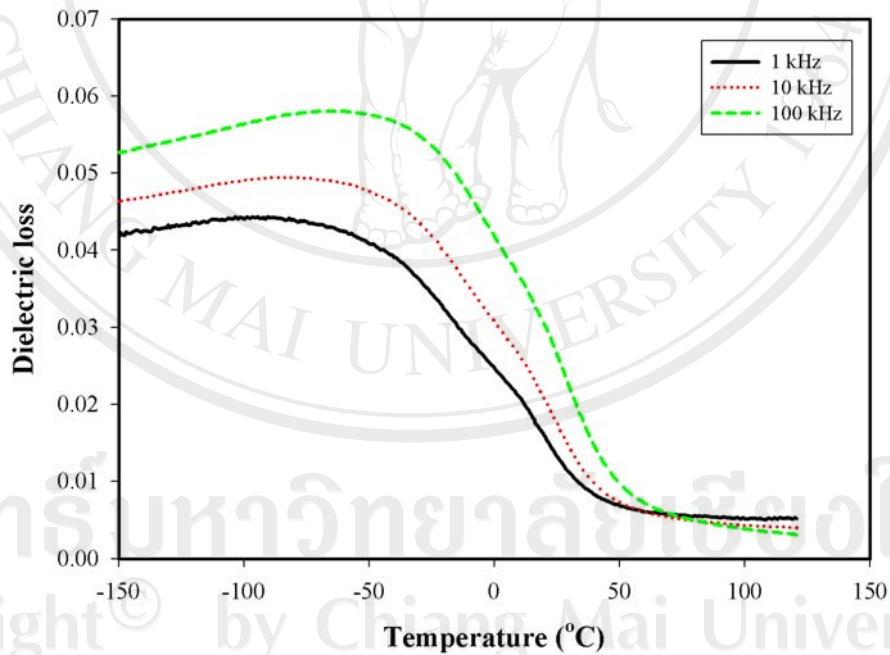
Table 6.4 Dielectric properties of $(1-x)$ PMN- x PT ceramic-nanocomposites.

x	Dielectric properties ^a							
	1100 °C				1250 °C			
	T_C (°C)	$\epsilon_{r,25 C}$	$\epsilon_{r,max}$	Tan δ_{max}	T_C (°C)	$\epsilon_{r,25 C}$	$\epsilon_{r,max}$	Tan δ_{max}
0.1	33	788	794	0.044	39	6224	6613	0.011
0.3	154	2514	8539	0.030	158	2807	13048	0.008
0.5	270	475	4433	0.055	268	820	7980	0.155

^aMeasured at 1 kHz

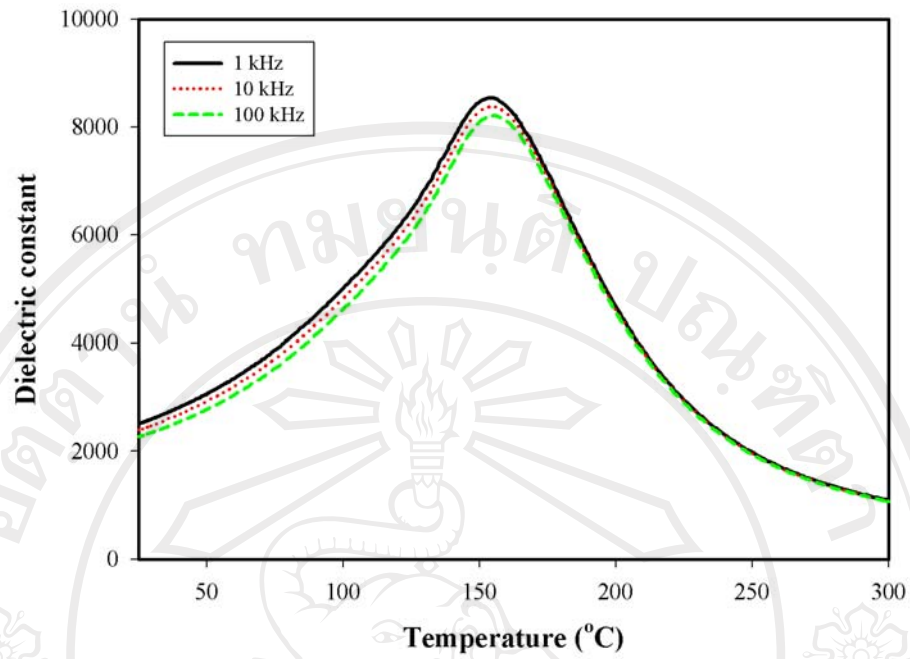


(a)

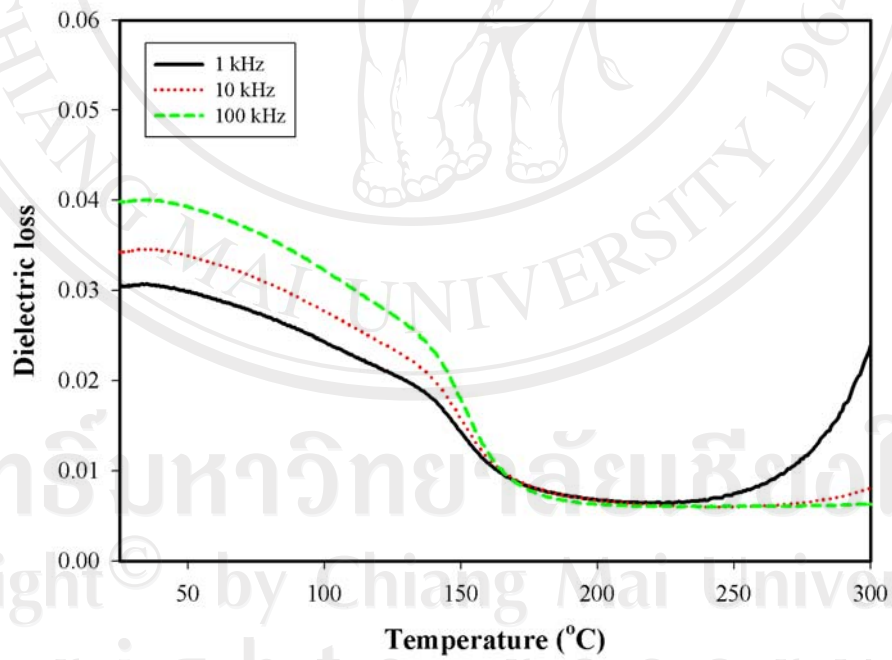


(b)

Fig. 6.16 Temperature and frequency dependences of dielectric properties of the (1-x)PMN-xPT ceramic-nanocomposites sintered at 1100 °C, (a and b) $x = 0.1$, (c and d) $x = 0.3$ and (e and f) $x = 0.5$.

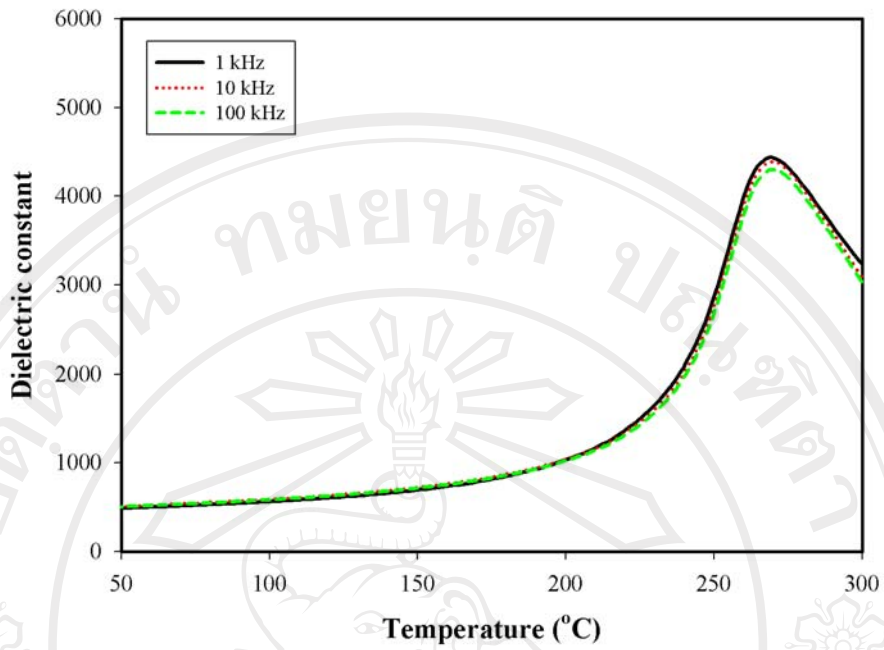


(c)

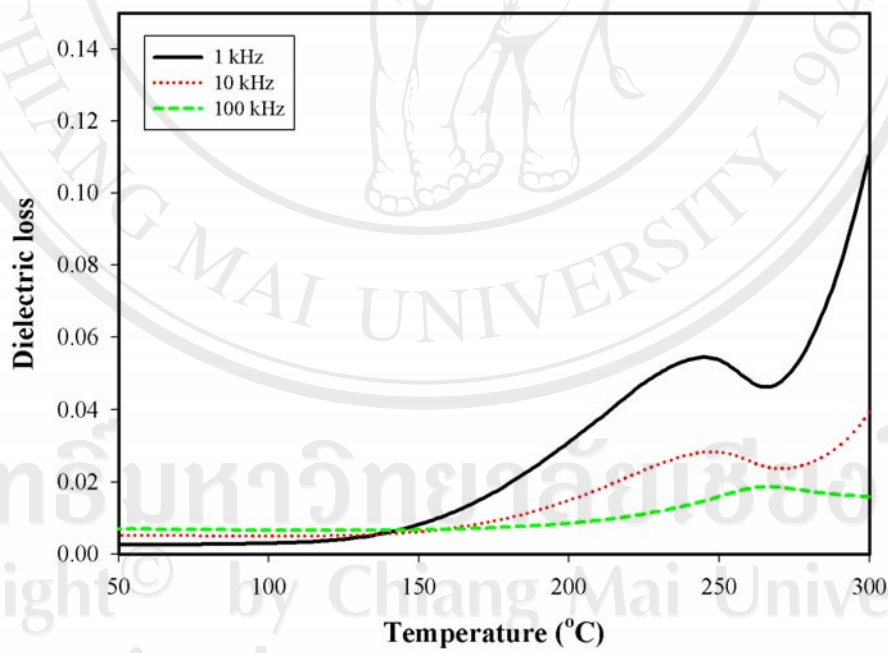


(d)

Fig. 6.16 (continued)

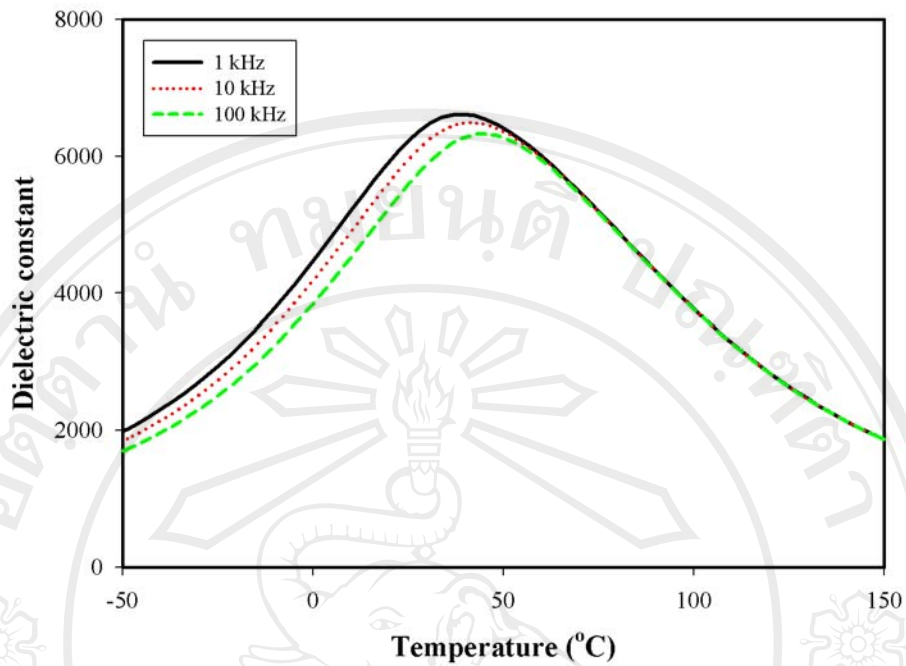


(e)

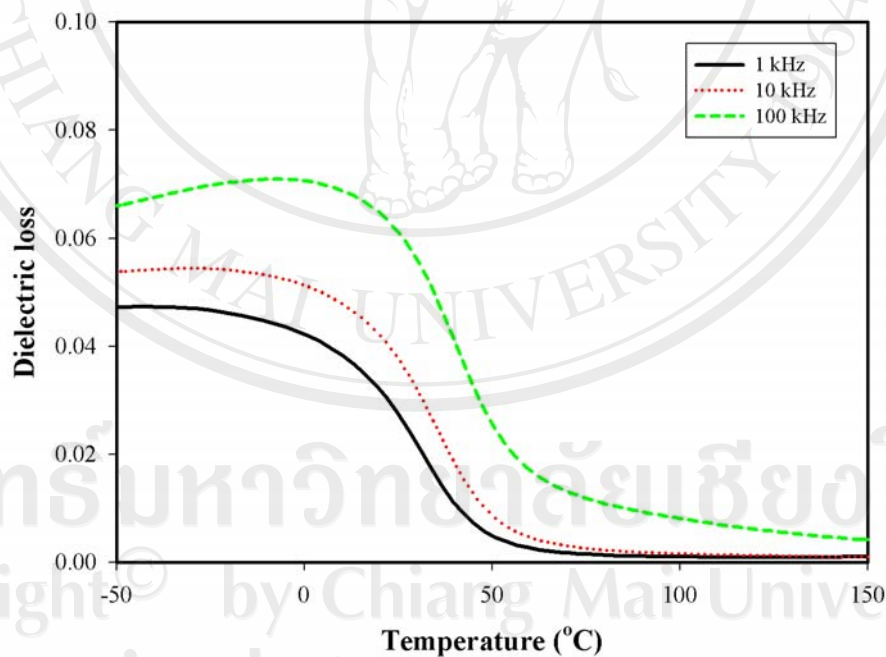


(f)

Fig. 6.16 (continued)

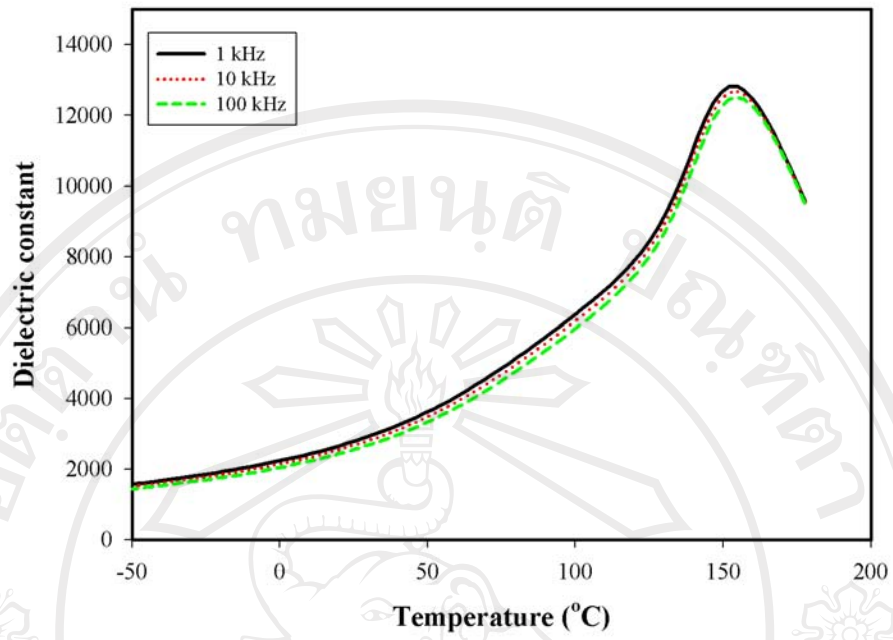


(a)

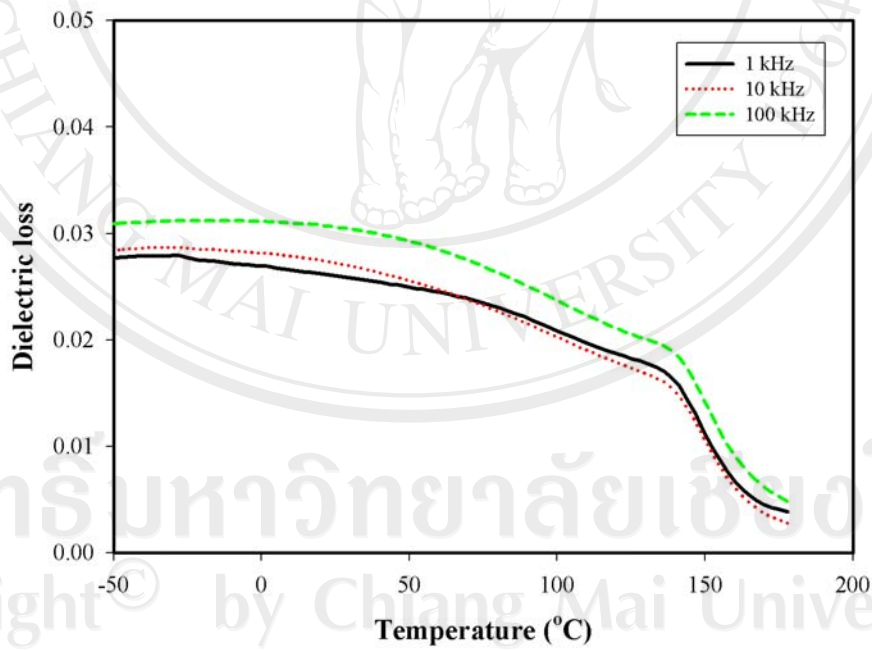


(b)

Fig. 6.17 Temperature and frequency dependences of dielectric properties of the (1- x)PMN- x PT ceramic-nanocomposites sintered at 1250 °C, (a and b) $x = 0.1$, (c and d) $x = 0.3$ and (e and f) $x = 0.5$.

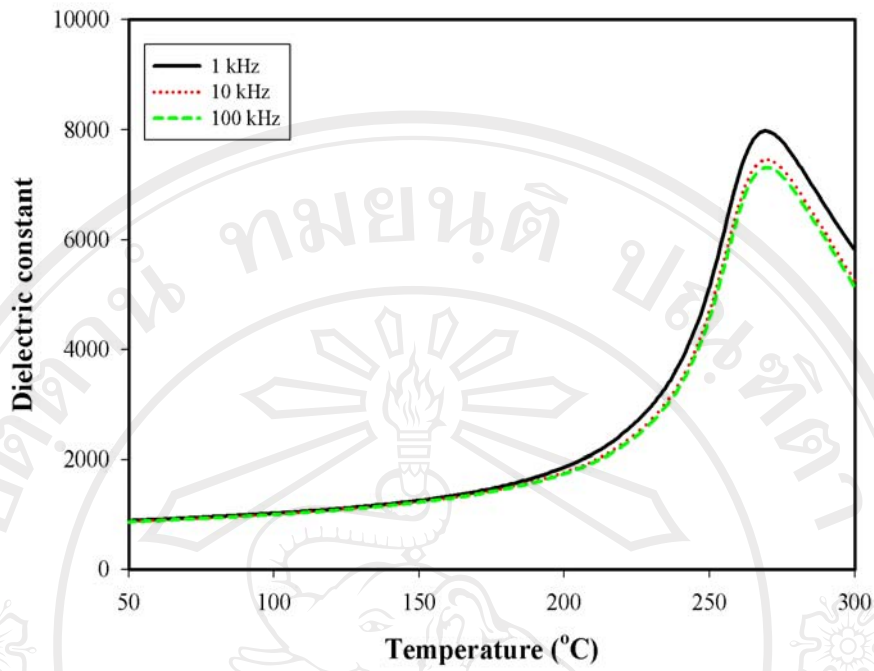


(c)

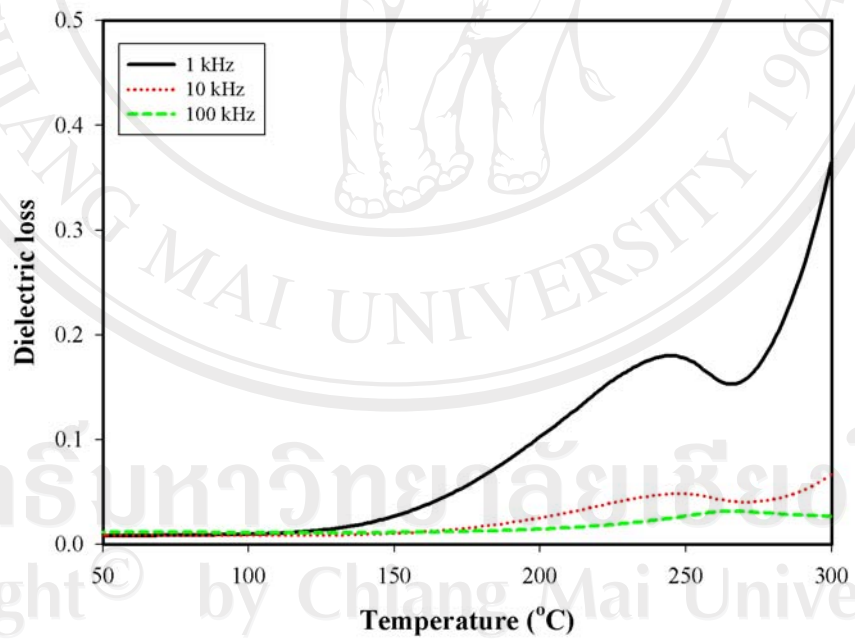


(d)

Fig. 6.17 (continued)



(e)



(f)

Fig. 6.17 (continued)

Fig. 6.18 illustrates a series of polarization-field (P - E) hysteresis loops for the PMN-PT ceramic-nanocomposites. It is clearly evident that the shape of P - E loops varies greatly with the ceramic compositions. With large amount of normal ferroelectric PT contents, the polarization loops of 0.5PMN-0.5PT and 0.6PMN-0.4PT are well developed showing large remnant polarization (P_r : remaining polarization when electric field is decreased to zero). The hysteresis loops are of a typical “square” form as a result of domain switching in an applied field. This is a typical characteristic of a phase that contains long-range interaction between dipoles in the ferroelectric micro-domain state [169]. This confirms that these compositions are of a normal ferroelectric phase with tetragonal symmetry, as indicated by the dielectric measurements and XRD analysis. The 0.7PMN-0.3PT ceramic shows largest polarization values with small coercive field (E_C), confirming that the composition is near the MPB of PMN-PT system. The other compositions with more PMN content show more of “slim” hysteresis loops, a characteristic of the suppressed ferroelectric interaction [169]. This is typically found in the relaxor ferroelectrics with polar nano-regions. This also has resulted in decreasing of the values of both P_r and E_C , as seen in Table 6.5, due to increased pseudo-cubic non-ferroelectric phase content [169,195].

Table 6.5 Ferroelectric properties of (1-*x*)PMN-*x*PT ceramic-nanocomposites.

<i>x</i>	Ferroelectric properties ^a		
	P_{Sat} (mC/m ²)	P_r (mC/m ²)	E_C MV/m
0.1	100	13	0.196
0.2	160	55	0.236
0.3	179	100	0.391
0.4	127.5	84	0.891
0.5	75	53	1.279

^bMeasured at 25 °C and 0.1 Hz

A similar behavior is also observed from the strain-electric field (*s-E*) relation, as plotted in Fig. 6.19. As can be seen, the near hysteresis-free electrostrictive behavior normally observed in relaxor ferroelectric is obtained in 0.9PMN-0.1PT ceramic. With increasing amount of PT, the *s-E* loops become more of “butterfly” type typically obtained in normal ferroelectric state. The field-induced strain increases with increasing amount of PT to 30 mol% (near MPB composition), reaching the maximum value of ~ 0.12%. Further increase in the PT content results in the decrease of the induced strain. Therefore, it can be concluded that the ferroelectric properties of the ceramics in PMN-PT system move gradually from the relaxor ferroelectric state in PMN to the normal ferroelectric state in 0.5PMN-0.5PT, crossing the MPB near 0.7PMN-0.3PT [169].

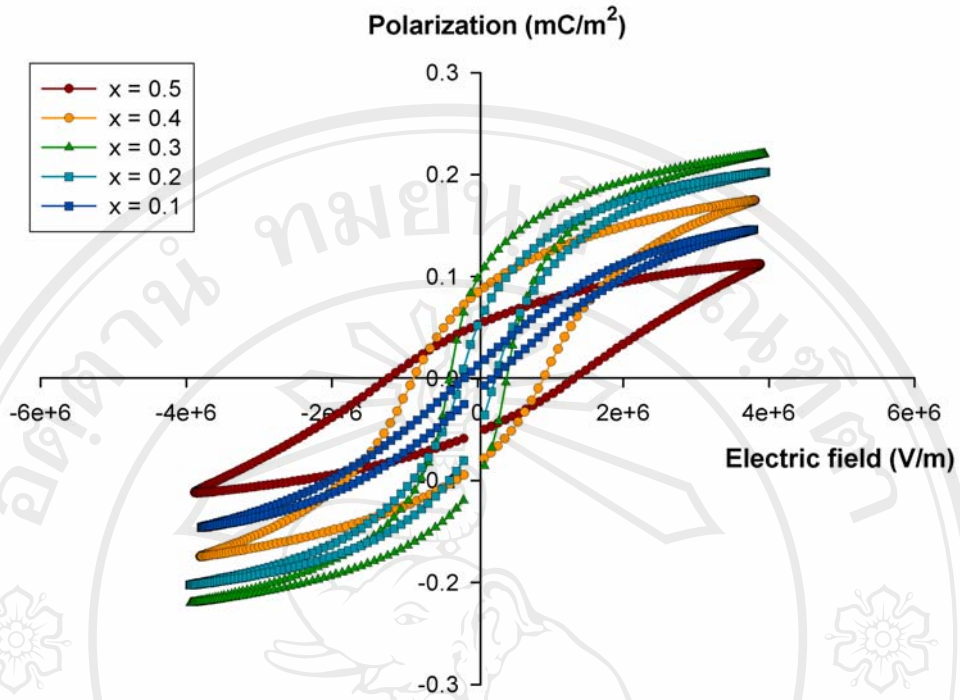


Fig. 6.18 P - E hysteresis loops of $(1-x)$ PMN- x PT ceramic-nanocomposites.

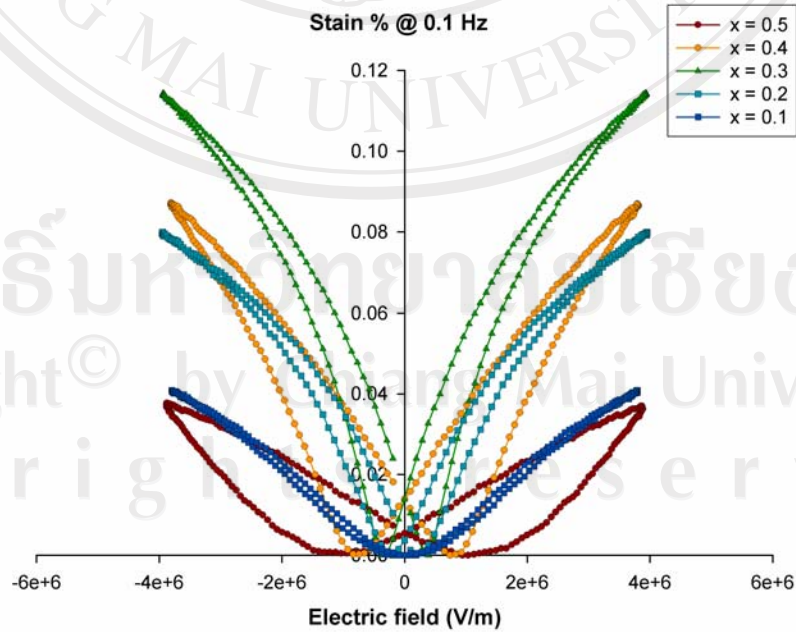


Fig. 6.19 s - E hysteresis loops of $(1-x)$ PMN- x PT ceramic-nanocomposites.

From the dielectric and ferroelectric data, the results and behavior seem like (1- x)PMN- x PT solid-solution with earlier publishes [189-191]. However, the values of ceramic-nanocomposites are slightly lower than solid solution values. It is possible that this lower ferroelectric data is due to the domain switching is prevented by the second phase particles which are incorporated within the matrix grains. Moreover, the dielectric behaviors still exhibit a broad peak in all composition. This behavior is different from solid-solution result (shows sharp peak with PT content increasing). It could be believed that there are two dielectric behaviors (relaxor ferroelectric and normal ferroelectric) exhibit in these samples.

The results of dilatometric measurements of (1- x)PMN- x PT ceramic-nanocomposites are presented in Fig. 6.20 (solid line is thermal expansion and dot line is thermal expansion coefficient). Table 6.6 lists the thermal expansion and transition temperature of PMN-PT compositions, derived from the thermal strain versus temperature measurements. Fig. 6.20 (a, b and c) indicate that the respective paraelectric-ferroelectric phase transition occurs at ~ 100 °C, 120 °C and 175 °C, for samples with $x = 0.2$, 0.3 and 0.35, respectively. The phase transition temperatures are consistent with literatures [40,197]. Most of these compositions exhibit low thermal expansion coefficient near the Curie temperature. The values of thermal expansion coefficient in the temperature range of -100 °C to 100 °C, as determined from heating cycle for 0.8PMN-0.2PT, 0.7PMN-0.3PT and 0.65PMN-0.35PT are 2×10^{-6} °C⁻¹, 2.4×10^{-6} °C⁻¹ and 3.2×10^{-6} °C⁻¹, respectively. Furthermore, the highest-temperature data, far above T_C , can be approximated by a straight line, as can be seen in the figures. The deviation from this linear high-temperature behavior occurs at 325 °C for $x = 0.2$, at 350 °C for $x = 0.3$ and at 360 °C for $x = 0.35$.

On analyzing the deviation of the strain from the high-temperature linear behavior and by using Eq. (3.8), P_d values can be obtained at various temperatures. Using the values of $Q_{11} = 0.123 \times 10^{-2} \text{ m}^4/\text{C}^2$ and $Q_{12} = -0.049 \times 10^{-2} \text{ m}^4/\text{C}^2$ [198] for $x = 0, 0.20, 0.30$ and 0.35 , P_d values can be calculated, as plotted in Fig. 6.21.

When calculating the spontaneous strains of the rhombohedral at a particular temperature, the cubic cell constant should be extrapolated to that temperature accounting for the thermal expansion. A linear extrapolation from above the transition temperature can be made over a narrow range with fairly good accuracy. In Fig. 6.21, we calculated the P_d , from $((P_d^2)^{1/2})$, values obtained from $\Delta l/l$. The normal reversible polarization data, P_r , determined from the P - E measurements is also plotted. It is evident that the polarization calculated from the strain is larger than P_r and extend several hundred degrees above T_m due to quadratic electrostrictive effects. Moreover, for temperatures well below T_m , although not equal, P_d and P_r are comparable; they are obtained by totally independent techniques. It has been known that the ferroelectric-paraelectric phase transition becomes more diffuse when the PT content decreases, indication of a more pronounced relaxor behavior. Ceramic with $x = 0.20$ shows more pronounced relaxor behavior, for which the P_d decays slowly with temperature compared to the other compositions ($x = 0.30$ and 0.35). Nevertheless, all $x = 0.20, 0.30$ and 0.35 show similar T_d value, even though there are differences in their compositions. These T_d values are several hundred degrees above the ferroelectric T_m (≈ 100 °C for $x = 0.2$, 120 °C for $x = 0.3$ and 175 °C for $x = 0.35$) indicating glassy polarization behavior over the range [199,200]. It seems that at $\approx T_d$ small local regions of the sample begin to show a polarization due to a favorable

arrangement of the atoms. The strain measurements can detect this effect because P_d^2 rather than P_d contributes to these terms. Once local regions of polarization occur, the cooperative effect that occurs at T_m can be understood.

Table 6.6 Various important features of the thermal expansion measurements in the selected PMN-PT ceramic-nanocomposites.

x	T_m (°C)	Thermal expansion coefficient ($\times 10^{-6} \text{ } ^\circ\text{C}^{-1}$) ^a	Calculated P_S at room temperature ($\mu\text{C}/\text{cm}^2$) ^b
0.2	100	2.0	94.58
0.3	120	2.4	56.33
0.35	175	3.2	54.76

^a The estimate precision of these value $\sim \pm 0.01\%$

^b The estimate precision of these value $\sim \pm 0.1\%$

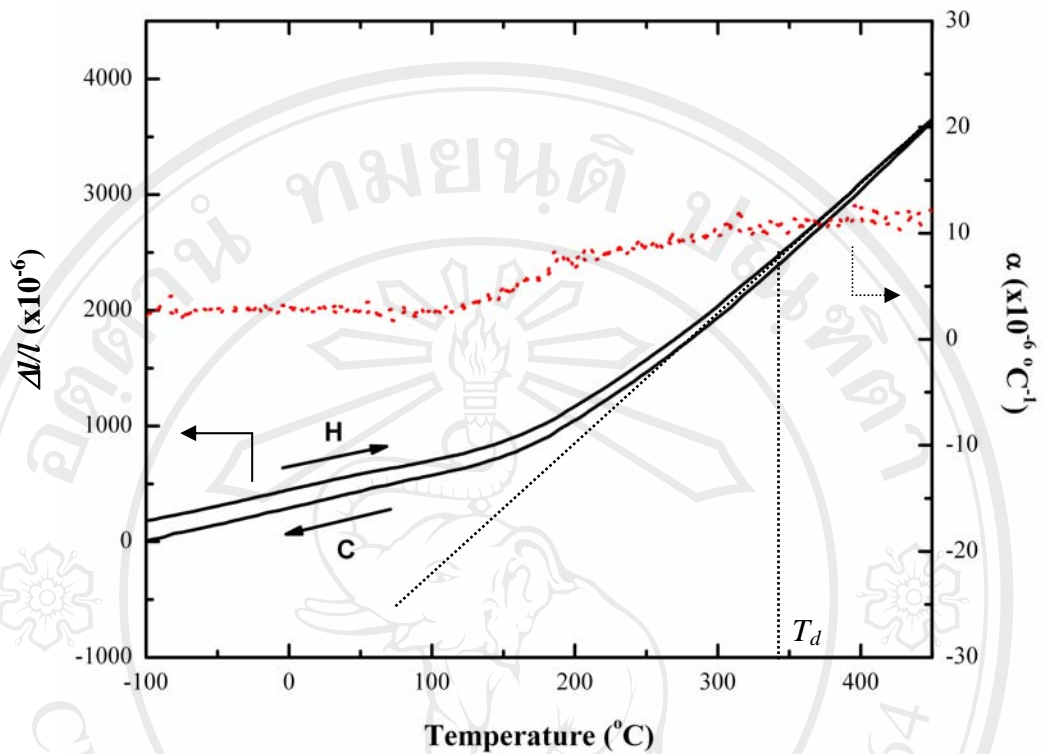


Fig. 6.20 Thermal expansion ($\Delta l/l$) and thermal expansion coefficient (α) as a function of temperature for (1- x)PMN- x PT ceramic-nanocomposites: (a) $x = 0.20$, (b) $x = 0.30$ and (c) $x = 0.35$.

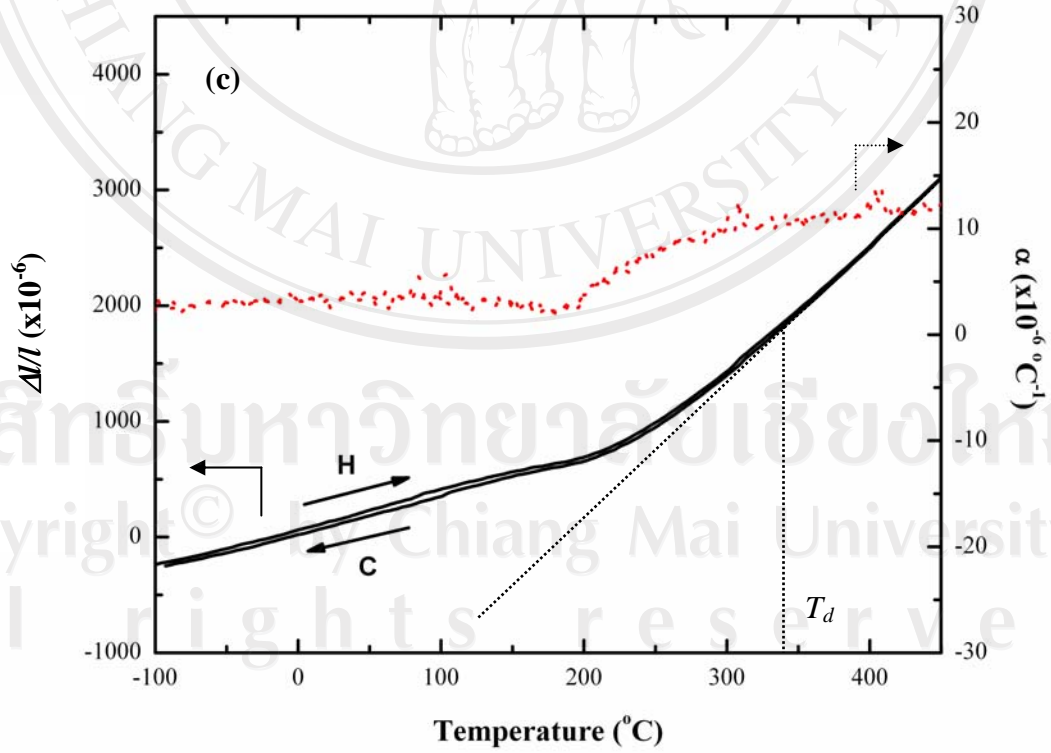
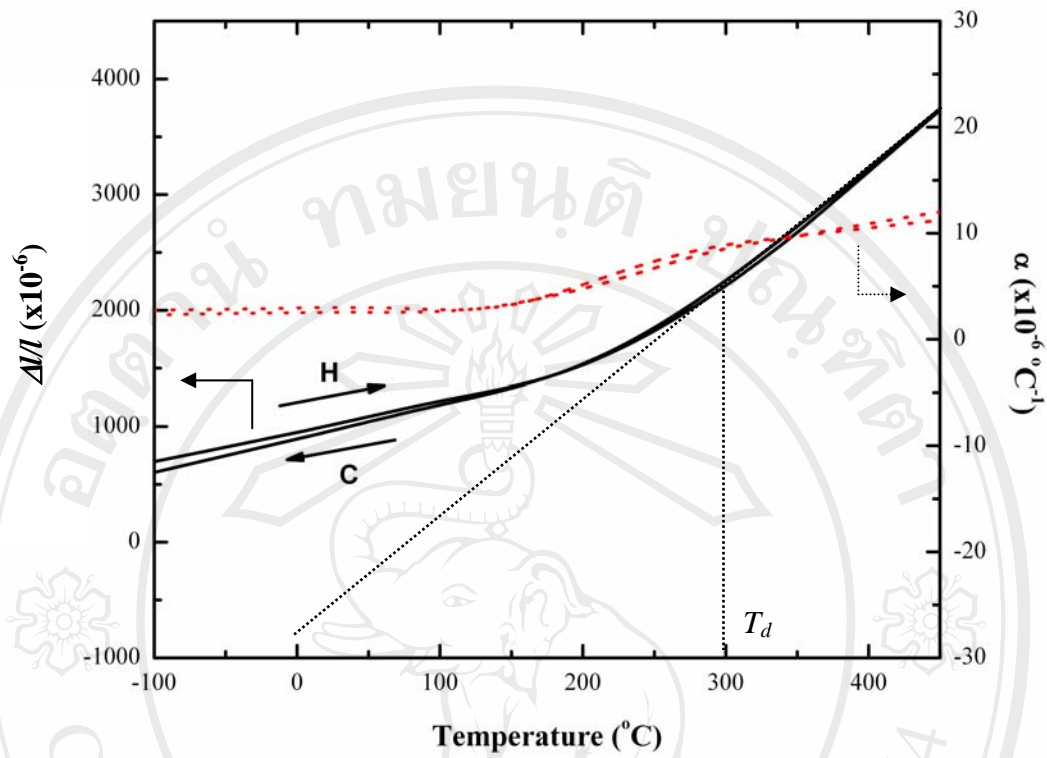


Fig. 6.20 (continued)

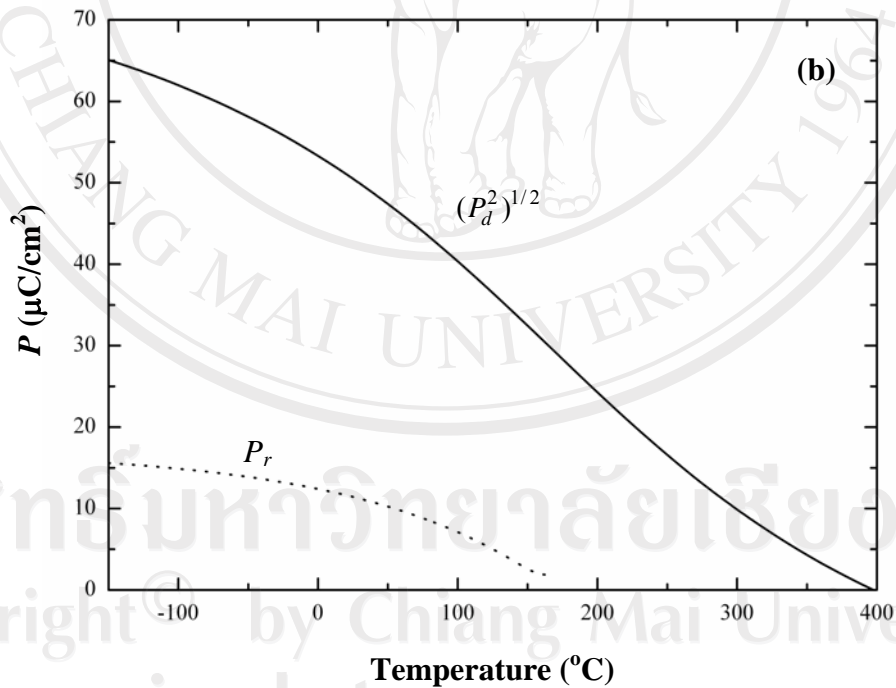
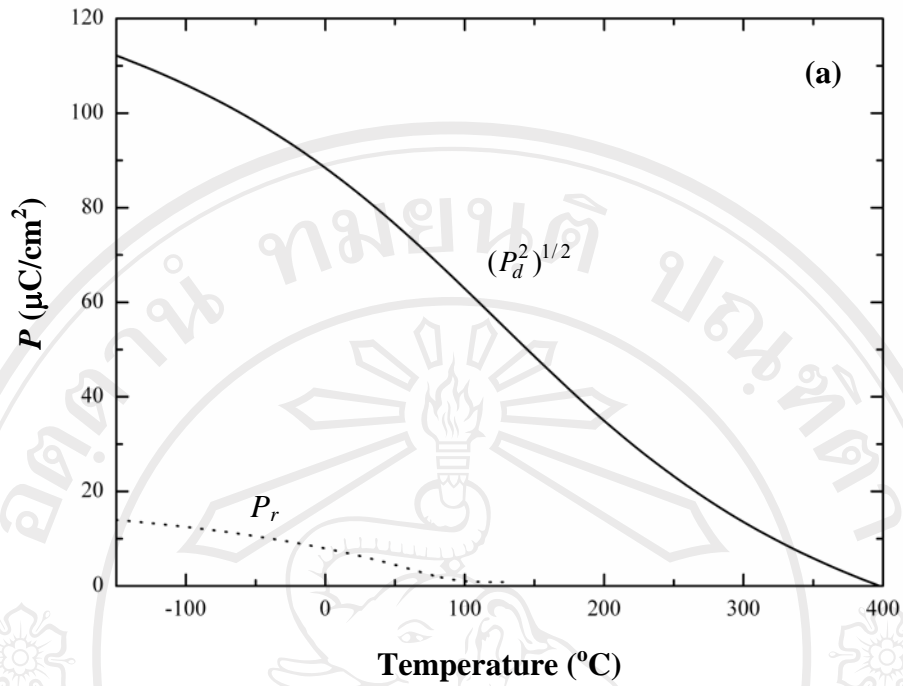


Fig. 6.21 $(P_d^2)^{1/2}$ as a function of temperature for (1-x)PMN-xPT ceramic-nanocomposites from Eq. (3.8) and the reversible ferroelectric polarizations P_r (dot lines): (a) $x = 0.20$, (b) $x = 0.30$ and (c) $x = 0.35$.

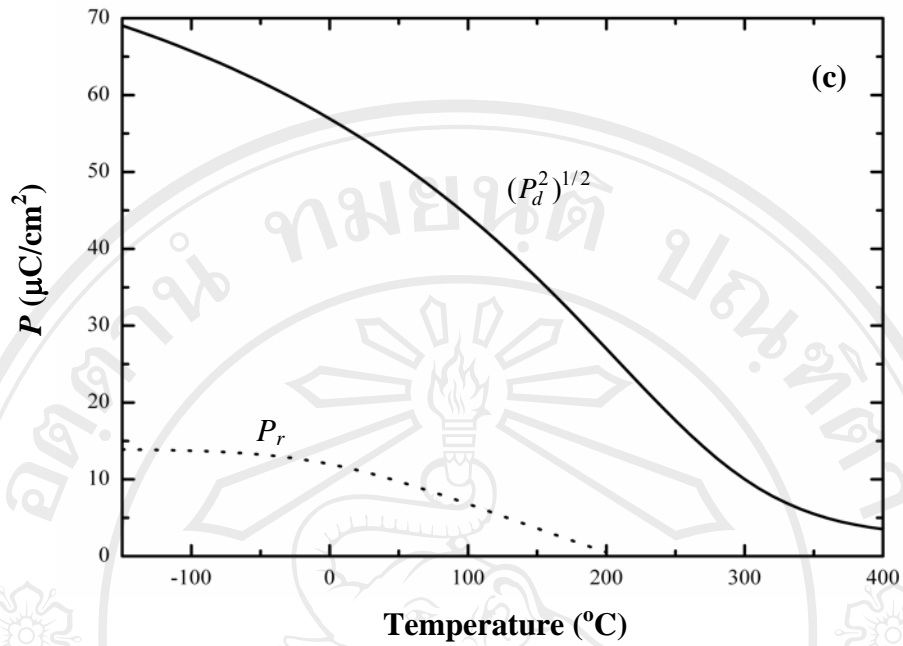


Fig. 6.21 (continued)

ลิขสิทธิ์มหาวิทยาลัยเชียงใหม่
 Copyright© by Chiang Mai University
 All rights reserved